Applied Computational Electromagnetics Society

# Express Journal

March 2016 Vol. 1 No. 3

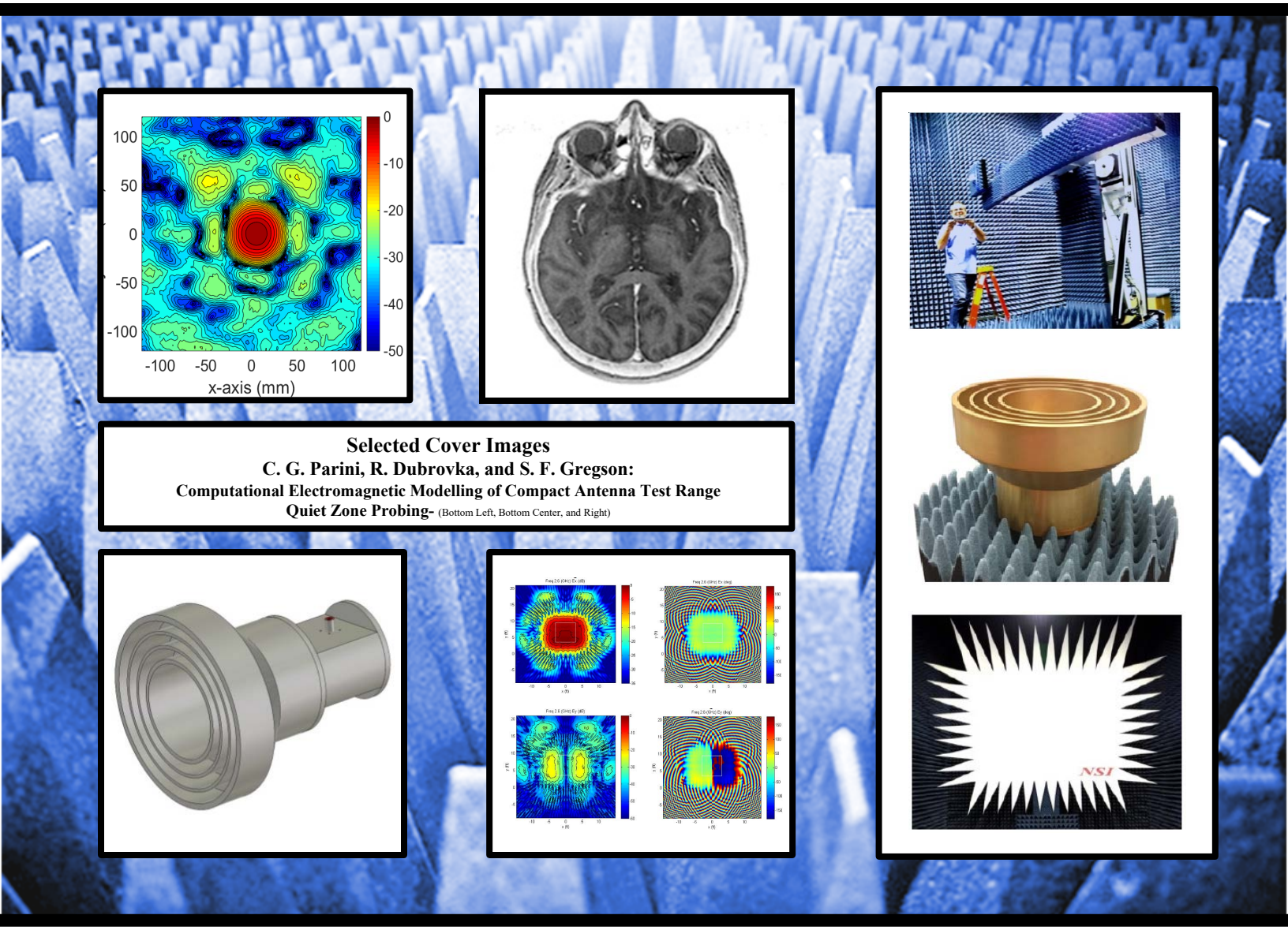


**Selected Cover Images**
**C. G. Parini, R. Dubrovka, and S. F. Gregson:**
**Computational Electromagnetic Modelling of Compact Antenna Test Range Quiet Zone Probing-** (Bottom Left, Bottom Center, and Right)

**APPLIED COMPUTATIONAL ELECTROMAGNETICS SOCIETY EXPRESS JOURNAL**

**http://aces-society.org**

## GENERAL INFORMATION

**PURPOSE AND SCOPE:** The Applied Computational Electromagnetics Society ***(ACES) Express*** Journal hereinafter known as the ***ACES Express Journal*** is devoted to the timely and rapid exchange of information in computational electromagnetics, to the advancement of the state-of-the art, and the promotion of related technical activities. The primary objective of the information exchange is to inform the scientific community in a short amount of time on the developments of recent computational electromagnetics tools and their use in electrical engineering, physics, or related areas. The technical activities promoted by this publication include code validation, performance analysis, and input/output standardization; code or technique optimization and error minimization; innovations in solution technique or in data input/output; identification of new applications for electromagnetics modeling codes and techniques; integration of computational electromagnetics techniques with new computer architectures; and correlation of computational parameters with physical mechanisms.

**SUBMISSIONS:** The ***ACES Express Journal*** welcomes original, previously unpublished papers, relating to applied computational electromagnetics. Typical papers will represent the computational electromagnetics aspects of research in electrical engineering, physics, or related disciplines as well as research in the field of applied computational electromagnetics.

Manuscripts are to be submitted through the upload system of ***ACES*** web site http://aces-society.org Please see "Information for Authors" on inside of back cover and at ***ACES*** web site. For additional information contact the Editor-in-Chief:

**Dr. Ozlem Kilic**
Department of Electrical Engineering and Computer Science
The Catholic University of America
Washington, DC 20064
Email: kilic@cua.edu

**SUBSCRIPTIONS:** All members of the Applied Computational Electromagnetics Society are entitled to access and download the ***ACES Express Journal*** of any published journal article available at http://aces-society.org. ***ACES Express Journal*** is an online journal and printed copies are not available. Subscription to ACES is through the web site.

***LIABILITY.*** Neither ***ACES***, nor the ***ACES Express Journal*** editors, are responsible for any consequence of misinformation or claims, express or implied, in any published material in an ***ACES Express Journal*** issue. This also applies to advertising, for which only camera-ready copies are accepted. Authors are responsible for all information contained in their papers. If any material submitted for publication includes material which has already been published elsewhere, it is the author's responsibility to obtain written permission to reproduce such material.

# THE APPLIED COMPUTATIONAL ELECTROMAGNETICS SOCIETY EXPRESS JOURNAL

Vol. 1 No. 3 March 2016

## TABLE OF CONTENTS

"Half-Loop Segmented Antenna with Omnidirectional Hemispherical Coverage for Wireless Communications"
Payam Nayeri, Atef Z. Elsherbeni, Roger Hasse, and Darko Kajfez……..88

"Computational Electromagnetic Modelling of Compact Antenna Test Range Quiet Zone Probing"
Clive G. Parini, Rostyslav Dubrovka, and Stuart F. Gregson……..92

"Enhanced Artificial Immune System Algorithm and Its Comparison to Bio-Inspired Optimization Techniques for Electromagnetics Applications"
Ozlem Kilic and Quang M. Nguyen…….……...97

"Experimental Benchmarking of Unstructured Transmission Line Modelling (UTLM) Method in Modelling Twisted Wires"
Xuesong Meng, Phillip Sewell, Nur H. A. Rahman, Ana Vukovic, and Trevor M. Benson……..101

"Four-Stage Split-Step 2D FDTD Method with Error-Cancellation Features"
Theodoros T. Zygiridis, Nikolaos V. Kantartzis, and Theodoros D. Tsiboukis……..…….105

"A 3-D Polynomial-Chaos FDTD Technique for Complex Inhomogeneous Media with Arbitrary Stochastically-Varying Index Gradients"
Georgios G. Pyrialakos, Theodoros T. Zygiridis, and Nikolaos V. Kantartzis…….109

# Half-Loop Segmented Antenna with Omnidirectional Hemispherical Coverage for Wireless Communications

**Payam Nayeri [1], Atef Z. Elsherbeni [1], Roger Hasse [2], and Darko Kajfez [3]**

[1] Department of Electrical Engineering and Computer Science
Colorado School of Mines, Golden, CO 80401, USA
pnayeri@mines.edu, aelsherb@mines.edu

[2] Georgia Tech Research Institute
Georgia Institute of Technology, Atlanta, GA 30332, USA
roger.hasse@gtri.gatech.edu

[3] Department of Electrical Engineering
University of Mississippi, University, MS 38677, USA
eedarko@olemiss.edu

***Abstract*** ─ Segmented antennas loaded with reactance elements at the junctions between segments provide additional parameters for shaping antenna characteristics. The design procedure consists of first, circuit analysis of the multiport antenna description to determine the initial values of the lumped element reactances and second, of fine tuning the antenna dimensions full-wave simulation software. Measured results show that a good matching and an omnidirectional radiation pattern in the vertical plane is maintained up to $\theta$ = 70º with a circular ground plane of 1m diameter.

***Index Terms*** ─ Antenna directivity, antenna impedance matrix, design optimization, omnidirectional antenna, partitioned antenna, printed circuit antenna, segmented antenna.

## I. INTRODUCTION

Many applications of wireless communication require antennas that provide omnidirectional radiation patterns. For example, an antenna designed for communication with non-stationary low-earth-orbit satellites should display an omnidirectional pattern in the upper half plane of a spherical system of coordinates. One possibility of creating such a radiation pattern is with the use of a half-loop segmented antenna [1] that can easily be fabricated in a printed-circuit form. As this antenna creates a linearly polarized field, a combination of two orthogonal antennas driven in ~~a~~ phase quadrature would be necessary for achieving circularly polarized radiation. This paper presents a new design of segmented half loop antenna that achieves omnidirectional radiation above a ground plane in one azimuthal plane.

The need for segmentation can be best understood by considering the characteristics of a solid (unsegmented) antenna such as shown in Fig. 1. We assume that the antenna circumference 2a is approximately one-half wavelength, and the two generators are in phase opposition. A transmitting loop antenna placed above a perfectly conducting ground plane as shown in Fig. 1, produces the same field in the upper half-space as another double-sized, full-loop antenna, located in free space. To distinguish the antenna in Fig. 1 from other loop antennas, we will call it a *half-loop* antenna.

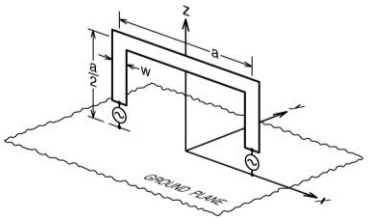


Fig. 1. A solid half-loop antenna above a perfectly conducting ground plane.

The directivity pattern created by such antenna is well known in the literature as is not shown for brevity. This pattern differs significantly from an ideal radiation pattern produced by an elementary magnetic dipole placed in the horizontal direction. In particular the directivity pattern of such an antenna drops by 5 decibels already at an angle of $\theta$ = 60º, instead of being constant up to the horizon as in the case of the elementary dipole. Note that in spherical system of coordinates, angle $\theta$ is counted from the vertical z axis. On the other hand, when the half-loop antenna of the

*Submitted On: June 24, 2015*
*Accepted On: January 31, 2016*

same overall dimensions is partitioned into 7 total segments, separated by lumped reactances, the simulated radiation pattern becomes as shown in Fig. 2, which is almost identical with an ideal magnetic dipole pattern. In addition, the segmented antenna is better matched than the solid version. More details about the segmentation procedure will be provided in Section III. This pattern has been obtained by the use of the full wave EM simulation software Ansys HFSS [2], assuming an infinite ground plane.

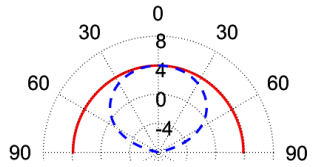


Fig. 2. Simulated directivity patterns of half-loop segmented antennas. The solid and dashed lines correspond to the *xz* and *yz* planes, respectively.

## II. EQUIVALENT CIRCUIT OF THE HALF-LOOP SEGMENTED ANTENNA

For a half-loop antenna with electrical length no greater than one-half wavelength, the radiation pattern could be made omnidirectional in the orthogonal plane, if one could maintain a stationary phase of the current distribution along the antenna conductor. The control of the current distribution along the antenna will be accomplished by segmenting the half-loop antenna into 7 segments as shown in Fig. 3. Without the loss of generality, the substrate used for the loop is a 32 mil Rogers RO4003 laminate.

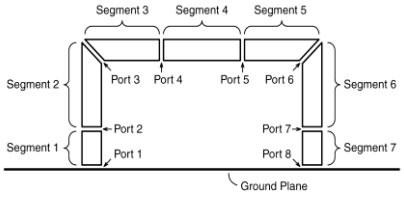


Fig. 3. The conductor of a half-loop antenna in Fig. 1 is divided into 7 segments.

Between each two neighboring segments a lumped reactance will be inserted leading to an equivalent circuit as shown in Fig. 4. From the circuit theory point of view, we see two impedance matrices; the antenna is described by matrix $\boldsymbol{Z_a}$ while the "external" reactances constitute diagonal impedance matrix $\boldsymbol{Z_{ex}}$:

$$\boldsymbol{Z_{ex}} = diag(0, jX_2, jX_3, \ldots jX_7, 0). \quad (1)$$

The capacitive reactances are negative, and inductive reactances are positive. In order to insure that the radiation in the positive *x* direction is of the same intensity as the one in the negative *x* direction, the reactance values should be made symmetric around the *z* axis, i.e., $X_2=X_7$, $X_3=X_6$ and $X_4=X_5$. Furthermore the source voltages should be made equal to each other ($V_{g1} = V_{g8}$). Then, the two input impedances will be equal to each other ($Z_{in1} = Z_{in8}$), and the two powers delivered to the antenna ports will also be equal to each other ($P_{in1} = P_{in2}$). Considering the structure in Fig. 3 to be an array comprised of 7 elements, the impedance matrix $\boldsymbol{Z_a}$ can be generated using full-wave electromagnetic simulation software [2].

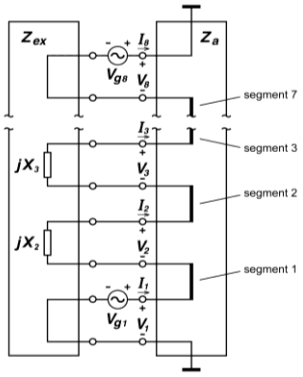


Fig. 4. Equivalent circuit of the half-loop segmented antenna.

When the voltages at the individual ports are grouped in the vector $|V\rangle$ and the port currents in a vector $|I\rangle$ the network in Fig. 4 is described by:

$$|I\rangle = (\boldsymbol{Z_a} + \boldsymbol{Z_{ex}})^{-1} |V_g\rangle. \quad (2)$$

The first component of vector $|V_g\rangle$ is equal to $V_{g1}$ and the 8th component is equal to $V_{g8}$ while the rest of components are being equal to zero. For the operation in the phase opposition, $V_{g1} = V_{g8}$, and it is therefore possible to evaluate the voltages and currents at all the ports. Thus, for any combination of reactances $X_2$ to $X_7$ it is possible to determine the *exact* input impedance with the use of circuit-theory Equation (2), without the need to refer to a full wave simulation software. Furthermore, it is also possible to *approximately* compute the radiation pattern based on the results obtained by the circuit theory as follows. Each of the segments is considerably shorter than the free-space wavelength, so one can assume that the current distribution along an individual segment will not display significant fluctuations. Thus, it is reasonable to assume that the current on the segment *i* is equal to the average value of port currents entering and exiting that segment:

$$I_{si} = (I_i + I_{i+1}) / 2. \quad (3)$$

The antenna system in Fig. 3 can be viewed to represent an array of known linear current sources $I_{si}$, so

that it is possible to evaluate the total radiated field using antenna theory [3]. It is convenient to define current moments as follows:

$$I_{mi} = \frac{2\pi d_i}{\lambda} I_{si}, \tag{4}$$

where $d_i$ is the length of the segment $i$ and λ is the free space wavelength. When the segments $i$ ($i$ = 1 to 7) are rotated by angles $\gamma_i$ with respect to the z-axis, their centers being located in the xz-plane at coordinates $x_i$ and $z_i$, the general formula for directivity in the xz plane becomes:

$$D(\theta) = \frac{7.5}{P_{in1}} \left| \sum_{i=1}^{14} \mathrm{I}_{mi} \sin(\theta - \gamma_i) e^{jk(x_i \sin\theta + z_i \cos\theta)} \right|^2. \tag{5}$$

Figure 5 displays the individual current moments that are used for computing the directivity. Although there are only 7 physical segments on the antenna, there are also 7 images below the ground plane that must be added in the summation (5). It is important to note that the number of segments needed for any given design is subjective. In the proposed design initially 5 segments were considered, however it was observed that adding segments on the top corners were necessary, hence this number was increased to 7. While adding more segments is also possible, due to added complexity it should generally be avoided.

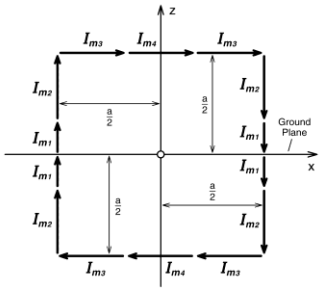


Fig. 5. The positions and orientations of the current moments on the segmented half-loop antenna.

## III. OPTIMIZATION PROCEDURE FOR INDIVIDUAL REACTANCES

Expression (5) enables one to estimate the radiation pattern as a function of $\theta$. For optimization purposes, directivity $D$ is evaluated at a number of $\theta$ points. Afterwards, the mean value $mD$ and the standard deviation $sD$ of all the points are computed. The objective function for optimization is then selected to be:

$$U = \frac{w_1}{mD} + w_2 \cdot sD + w_3 \cdot \rho. \tag{6}$$

In this way, the mean directivity is maximized, the standard deviation of directivity (i.e., the departure from the omnidirectional shape) is minimized, and the input reflection coefficient is minimized. The weight $w_1$ is used to emphasize the mean directivity; $w_2$ is used to emphasize the uniform directivity; and $w_3$ is used to emphasize the impedance match.

For demonstration and verification purposes, the side length of the half-loop from Fig. 6 is selected to be $a$ = 62 mm, and the strip width is 5 mm. The operating frequency is selected to be $f$ = 1.2276 GHz (GPS L2 band). The 8-port antenna impedance matrix is created by HFSS, while the initial optimization is performed with the Matlab® program "fminsearch" [4].

At the start of optimization, all reactances are set to be equal to -259 Ω (i.e., 0.5 pF). The three optimized reactances come out to be $X_2$= -500 Ω, $X_3$= 92.7 Ω and $X_4$= -432 Ω. Thus, the second and the fourth loading reactances are capacitive, while the third one is inductive. The amplitudes and phases of the current moments at the start of optimization are shown in Fig. 6 (a), and after optimization they are shown in Fig. 6 (b). It can be seen that the amplitudes of the current moments after optimization have become several times larger, because of an improved impedance match. The phase distribution has also changed somewhat after optimization, but phases still remain close to each other. The predicted mean directivity is $mD$= 3.6 dBi, and the predicted input return loss is 20 dB.

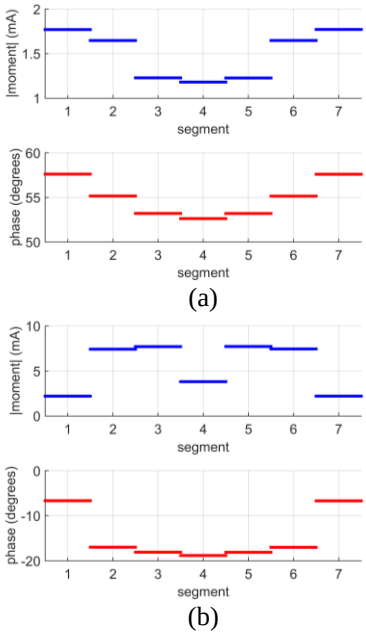


Fig. 6. Amplitudes and phases of current moments on individual segments: (a) before optimization, and (b) after optimization.

When the optimized values of lumped reactances are inserted in the antenna model, the radiation pattern obtained by HFSS is shown in Fig. 2 (b). As expected, the shape of the pattern closely resembles that of an ideal magnetic moment oriented along the y axis. As far as the directivity of this oversized magnetic dipole is concerned, the directivity value computed by HFSS is

slightly larger than the 3.6 dBi predicted by circuit analysis, namely 4.1 dBi in the z direction, and it drops to 3.8 dBi in the x direction. The simulated return loss is approximately 21.6 dB at 1.2276 GHz, which is in good agreement with the value obtained by circuit theory of 20 dB at 1.2276 GHz.

The final step is to model the required reactances of the segmented antenna. The inductance corresponding to $X_3$ is $L_3$=12.03 nH. This value is realized by a small circular loop in each of the two corners of the half-loop. The trace width for this inductor was set to 1 mm. The other two lumped elements are capacitances 0.26 and 0.30 pF, which are realized by overlapping the strips located on the opposite sides of the substrate. For these three sets of printed reactive elements, the initial dimensions were determined based on static approximation. The final dimensions, i.e., the loop radius for the inductors and overlap length for the capacitors, were determined with direct optimization of these parameters in the full-wave software. This secondary optimization resulted in an omnidirectional directivity of 3.8 dBi in both x and z directions, with the input reflection coefficient magnitude of -21.6 dB at 1.2276 GHz. The dimensions for the inductive loop radius, and the overlap capacitor lengths, were 2.22 mm, 1.55 mm, and 1.95 mm, respectively. The printed circuit arrangement, and a photo of its prototype, are shown in Fig. 7. A lumped port excitation was used in the simulation model to represent the SMA end-launch connector of the fabricated prototype. The substrate used for the ground plane and feed network is a 62 mil Rogers RT/Duroid 5880. Note that the feed network is a power divider which feeds the two ports of the HLA out of phase [1].

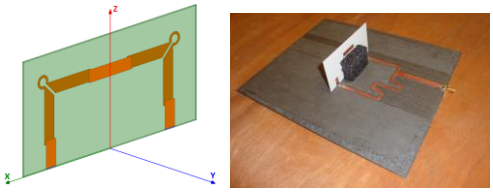


(a) (b)

Fig. 7. (a) Printed circuit version of the antenna. (b) Half-loop segmented antenna prototype.

## IV. PROTOTYPE MEASUREMENTS

The radiation pattern measured with a ground plane of 1 meter diameter is compared with the simulated pattern in Fig. 8. The antenna radiation pattern and efficiency were measured using the SG64 Starlab measurement system at Kennesaw, GA. Because of the limited ground plane size, the edge diffraction effect is clearly visible. The measured value drops below the simulated value at $\theta$ = 70º. For a larger ground plane size, one would expect-wider omnidirectional coverage angle. The measured radiation efficiency at the center frequency is 93%. The measured reflection coefficient magnitude is given in Fig. 9.

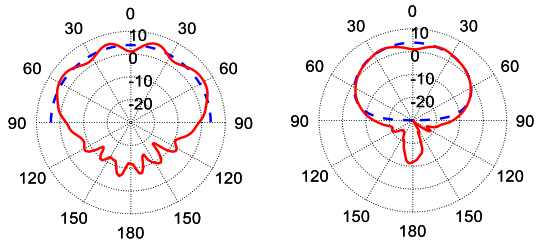


(a) (b)

Fig. 8. Measured (solid) and simulated (dashed) radiation patterns of the antenna at 1.2276 GHz in: (a) *xz* or $\varphi$ = 0º and (b) *yz* or $\varphi$ = 90º planes.

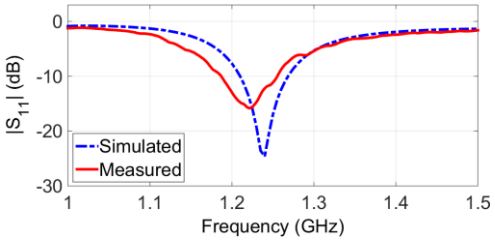


Fig. 9. Reflection coefficient magnitude of the antenna.

## V. CONCLUSIONS

By allowing the individual reactances in a segmented antenna to take distinct values, it becomes possible to simultaneously optimize the radiation pattern and the input match of the antenna. A preliminary optimization is considerably speeded up by analyzing the antenna equivalent circuit. The required capacitances and inductances can be easily integrated into the printed circuit of the segmented antenna, such that no external matching circuit is necessary.

## ACKNOWLEDGMENT

The authors would like to thank Microwave Vision Group (MVG) and Satimo USA for the measurement of segmented antennas using the SG64 Starlab system at Kennesaw, GA, and to Ansys Inc. for their software package donation to Colorado School of Mines.

## REFERENCES

[1] P. Nayeri, D. Kajfez, and A. Z. Elsherbeni, "Design of a segmented half-loop antenna," *IEEE Antennas and Propagation Society International Symposium*, Memphis, TN, July 2014.

[2] ANSYS HFSS, v. 15.0, ANSYS Inc.

[3] R. E. Collin, *Radiation from Simple Sources*, Ch. 2, Antenna Theory, Part I, New York: McGraw-Hill, 1969.

[4] Matlab®, The Mathworks Inc., Natick, MA.

# Computational Electromagnetic Modelling of Compact Antenna Test Range Quiet Zone Probing

**C. G. Parini [1], R. Dubrovka [1], and S. F. Gregson [2]**

[1] School of Electronic Engineering and Computer Science
Queen Mary University of London, London, E1 4FZ, UK
c.g.parini@qmul.ac.uk, r.dubrovka@qmul.ac.uk

[2] Nearfield Systems Inc.
19730 Magellan Drive, Torrance, CA, 90502, USA
sgregson@nearfield.com

***Abstract*** ─ This paper extends the authors previous simulation study [1, 2] that predicted the quality of the pseudo plane wave of an offset compact antenna test range (CATR). In this paper, the quiet-zone performance predictions are extended to rigorously incorporate the effects of probing the CATR quiet-zone using various field probes. This investigation leads to recommendations as to the optimal field probe choice and measurement uncertainties. The results of these new simulations are presented and discussed.

***Index Terms*** ─ Compact antenna test range, field-probe, quiet-zone probing, reaction theorem.

## I. INTRODUCTION

The single-offset compact antenna test range (CATR) is a widely deployed measurement technique for the broadband characterization of electrically large antennas at reduced range lengths. The CATR collimates the quasi-spherical wave radiated by a low gain feed into a pseudo transverse electric and magnetic (TEM) plane-wave. The coupling of this locally plane-wave into the aperture of an antenna under test (AUT) creates the classical measured "far-field" pattern. The accuracy of an antenna measured using a CATR is therefore primarily determined by the uniformity of the amplitude and phase of this illuminating pseudo plane-wave.

Traditionally, the quality of the pseudo plane wave has been assessed by "probing" the amplitude and phase across a transverse planar surface with the results being tabulation on, typically, a plane-polar grid consisting of a series of linear scans in the horizontal, vertical and perhaps inter-carinal planes. A number of workers have utilized portable planar near-field antenna test systems to acquire two-dimensional plane-rectilinear data sets that can be used to provide far greater insight into the behavior of the field in the quiet-zone (QZ) and additionally for the purposes of chamber imaging to provide angular image maps of reflections [3]. However, when mapping the CATR QZ the finitely large aperture of any realized field probe will inevitably affect the mapped fields by way of the convolution process between the pseudo plane wave of the CATR and the aperture illumination function of the scanning near-field probe, *cf.* [4] Potentially, such a discrepancy can lead to confusion when comparing CATR QZ predictions obtained from standard computational electromagnetic (CEM) models and empirical measurements as this "boxcar" field averaging process is not automatically incorporated within the numerical simulation. Several authors have undertaken CATR performance prediction modeling [7, 8, 9] with increasing levels of complexity. This paper extends our recently published comprehensive CATR QZ performance prediction software tool [1, 2] to incorporate the directive properties of several commonly used field probes so that recommendations can be made as to the most appropriate probe to use as well as providing estimates for the upper bound measurement uncertainty.

## II. CATR QZ SIMULATION

The field illuminating the CATR offset parabolic reflector is typically derived from the assumed known far-field pattern of the feed antenna. This pattern could be derived CEM simulation, as is the case here, or from empirical range measurements. Figure 1 contains a mechanical drawing of the WR430 choked cylindrical waveguide feed that was used during these simulations with the realised feed shown in Fig. 2. Here, the feed is assumed nominally vertically polarised within its local coordinate system. When computing CATR QZ simulations for a horizontally polarised feed a vector isometric rotation [4] can be used to rotate the probe by 90° about its local $z$-axis so as to produce equivalent far-field patterns for a horizontally polarised probe.

Figures 3 and 4 respectively illustrate the far-field

*Submitted On: August 20, 2015*
*Accepted On: July 7, 2016*

amplitude and phase cardinal cuts of the feed antenna when resoled onto a Cartesian polarisation basis. These patterns were obtained from a proprietary three-dimensional full-wave CEM solver that used the finite difference time domain (FDTD) method. Here, the difference in beam-widths is exacerbated by presenting the patterns resolved onto a Cartesian polarisation basis [4].

Fig. 1. Model of WR430 CATR feed.

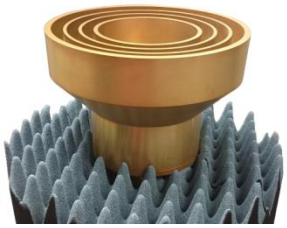

Fig. 2. Realised WR430 CATR feed.

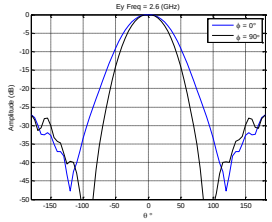


Fig. 3. Amplitude cardinal cuts of feed at 2.6 GHz.

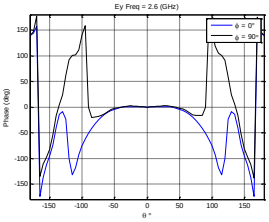


Fig. 4. Phase cardinal cuts of feed at 2.6 GHz.

The location of the phase centre was determined by means of a best fit parabolic function over the $-50° \le \theta \le 50°$ angular range [5]. The maximum polar angle of 50° was selected as this is the maximum angle subtended at the feed by the CATR parabolic reflector. For angles larger than this, the feed pattern spills over from the reflector and the feed pattern function for angles larger than this are unimportant. Here, the phase centre of this circular feed was determined as being at $x = y = 0$ m and $z$ = -0.1377 m and was found to be extremely stable across the operating bandwidth. The phase patterns were compensated for this parabolic phase function which conceptually corresponds to installing the phase centre of the feed at the focus of the CATR parabolic reflector. The field illuminating the parabolic reflector can then be determined from far-field antenna pattern function by reintroducing the (conventionally suppressed) spherical phase function and the inverse $r$ term. The corresponding magnetic field, as required by the field propagation algorithm, can be computed from the electric field from the TEM far-field condition [4].

As a result of the requirement to minimise feed induced blockage, as described in [1, 2], a single offset reflector CATR design is harnessed. Here, it is assumed that the vertex of the reflector is coincident with the bottom edge of the main reflector. Thus, the feed is required to be tilted up in elevation so that the boresight direction of the feed is orientated towards the centre of the reflector surface. In this case, the CATR main reflector is formed from an offset parabolic reflector with a focal length of 12' = 3.6576 m. The reflector was 4.71 m wide by 3.9 m high with serrations of 0.76 m in length. The following figure shows a false-colour plot of the magnitude of the illuminating electric field as radiated by the WR430 feed. Here, the boresight direction of the feed is pointing through the geometric centre of the reflector which corresponds to an elevation tilt angle of approximately 28°. Although this is a non-optimum illumination angle, in actuality a larger elevation angles is used to improve the CATR QZ amplitude taper by compensating for the spherical loss factor, this value was used for the sake of consistency with prior simulations [1, 2]. Within Fig. 5, the white space corresponds to regions where the reflectivity of the reflector is zero. Figure 6 shows an image of the reflector once installed within the test chamber.

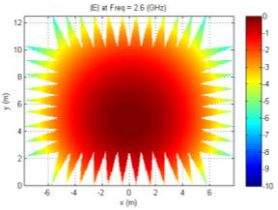


Fig. 5. Magnitude of incident electric field.

Fig. 6. Realised CATR main reflector.

The current element method [1, 2, 6] replaces fields with an equivalent surface current density $\underline{J}_s$ which is used as an equivalent source to the original fields. The surface current density across the surface of the reflector can be obtained from the incident magnetic fields and the surface unit normal using,

$$\underline{J}_s = 2\hat{\underline{n}} \times \underline{H}_i = 2\hat{\underline{n}} \times \underline{H}_r \,. \tag{1}$$

The surface current density approximation for $\underline{J}_s$ (as embodied by the above expression) is known as the physical-optics approximation and allows for the computation of valid fields outside of the deep shadow region. The infinitesimal fields radiated by an electric current element can be obtained from the vector potential and the free-space Green's function [1, 6],

$$d\underline{H}(P) = \frac{da}{4\pi} \underline{J}_s \times \nabla \psi \,. \tag{2}$$

This is an exact equation. When the field point is more than a few wavelengths from the radiating elemental source, the corresponding elemental electric fields can be obtained conveniently from the elemental magnetic fields using the far-field TEM condition using,

$$d\underline{E} = Z_0 \left( d\underline{H} \times \hat{\underline{u}} \right). \tag{3}$$

Thus, both the electric and magnetic fields can be obtained from the elemental fields by integrating across

the surface of the parabolic reflector. In practice, for the case of a CATR with a QZ located at a distance $z$ that is larger than the focal length of the reflector, the difference between the electric field as computed using the TEM condition and the exact formula is typically on the order of the limit of double precision arithmetic with this error being negligible. Figures 7 and 8 contain respectively false colour plots of the amplitude and phase patterns of the horizontally polarised electric field components of the pseudo-plane wave over the surface of a transverse plane located down-range at $z = 1.8f$, where $f$ is the focal length of the CATR reflector at a frequency of 2.6 GHz. Figures 7, 8, 9 and 10 contain the $E_x$ and $E_y$ polarised amplitude and phase patterns for the horizontally polarised feed case. Although not shown, the equivalent magnetic fields were also computed. When interpreting these plots it is important to recognise that these are the fields one would measure if an infinitesimal electric (*i.e.*, Hertzian) dipole probe were used to sample the QZ fields [4]. This is in agreement with theory and standard CEM modelling tools. In practice, it is not possible to use an infinitesimal current element as a field probe and the following section examines how these patterns can be modified to include the effects of a finitely large, *i.e.*, directive, field probe.

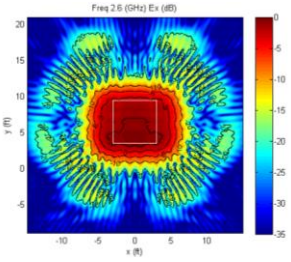


Fig. 7. $E_x$ polarised QZ electric field amplitude.

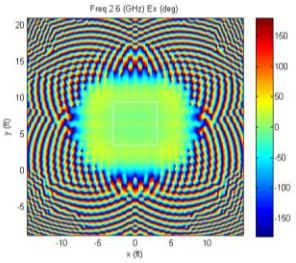


Fig. 8. $E_x$ polarized QZ electric field phase.

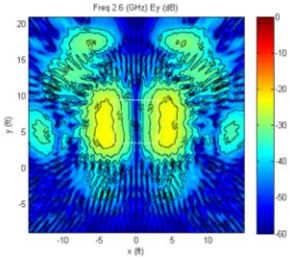


Fig. 9. $E_y$ polarized QZ electric field amplitude.

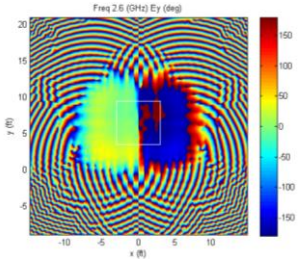


Fig. 10. $E_y$ polarised QZ electric field phase.

## III. CATR QZ PROBING SIMULATION

CATR QZ probing is usually accomplished by translating a field probe across a plane that is transverse to the z-axis of the CATR at several positions down-range. An example of a CATR QZ field probe can be seen presented in Fig. 11. Here, the electrically small field probe can be seen positioned at the limit of travel of the 6' linear translation stage. Generally, pyramidal horns, *e.g.*, *circa* 16 dBi standard gain horns (SGH) [6], are used as CATR QZ probes as they have excellent polarisation purity, are easy to align, have some gain and therefore provide some immunity from reflections from the side and back walls of the anechoic chamber. An alternative choice of field probe is a *circa* 6 dBi gain open ended rectangular waveguide probe (OEWG) [6].

Fig. 11. CATR QZ field being probed using a linear translation stage and a plane-polar acquisition scheme.

The clear difference in the electrical size of aperture of these two antennas and their directive properties and spatial filtering can be expected to result in some differences being observed between the probe measured QZ fields with the effects being quantifiable through an application of the reaction theorem which is a well-known method for analyzing general coupling problems [2, 4]. This theorem states that, provided the electric and magnetic field vectors ($\underline{E}_1$, $\underline{H}_1$) and ($\underline{E}_2$, $\underline{H}_2$) are of the same frequency and are monochromatic, then the mutual impedance, $Z_{21}$, between two radiators, *i.e.*, antennas 1 and 2, in the environment described by ε, μ can be expressed in terms of a surface integration [2, 4],

$$Z_{21} = \frac{V_{21}}{I_{11}} = -\frac{1}{I_{11} I_{22}} \int_{S_2} \left( \underline{E}_2 \times \underline{H}_1 - \underline{E}_1 \times \underline{H}_2 \right) \cdot \hat{\underline{n}} \, ds. \quad (4)$$

Here, $\underline{n}$ is taken to denote the outward pointing surface unit normal. The subscript 1 denotes parameters associated with antenna 1 whilst the subscript 2 denotes quantities associated with antenna 2, where the surface of integration encloses antenna 2, but not antenna 1. Here, $I_{11}$ is the terminal current of antenna 1 when it transmits and similarly, $I_{22}$ is the terminal current of antenna 2 when it transmits. Note that this integral does *not* compute transferred power as there are no conjugates present and as such, crucially, phase information is preserved. Here, the fields $\underline{E}_1$ and $\underline{H}_1$ are used to denote the CATR QZ whilst fields $\underline{E}_2$ and $\underline{H}_2$ denote fields associated with the QZ field probe. From reciprocity, the mutual impedance, $Z_{12} = Z_{21}$, is related to the coupling between the two antennas. Clearly the mutual impedance will also be a function of the displacement between the antennas, their relative orientations, their directivities and their respective polarization properties. Once the

impedance matrix is populated, this can be inverted to obtain the admittance matrix whereupon the required scattering matrix can be computed [4]. The elements $S_{1,2} = S_{2,1}$ of this two port scattering matrix are the complex transmission coefficients for the coupled antenna system which represent a single point in the quiet-zone probing measurement. Although the integration can be performed across any convenient free-space closed surface, in this application integrating across the planar aperture of the OEWG or SGH antenna is perhaps the most computationally efficient strategy. Aperture fields can be obtained from analytical models [4] as in this case, from CEM simulation [4] or from measurement with the choice being determined by the accuracy needed and the available information.

Figure 12 presents a comparison of the CATR QZ amplitude horizontal cut as obtained using an infinitesimal electric dipole (red trace) and an equivalent cut as obtained by using an OEWG probe (blue trace). A measure of the similarity between the respective measurements is provided by the equivalent multipath level (EMPL) [4] (magenta trace). From inspection of Figs. 12 and 13, it is evident that the ideal (dipole) and OEWG measurements are in very good agreement, both in amplitude and phase for the horizontal cuts. This is further confirmed by the EMPL level that is at or below -60 dB right across the pattern peak which corresponds to the useable QZ region.

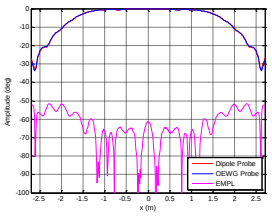


Fig. 12. Horizontal amplitude cut using dipole and OEWG field probe.

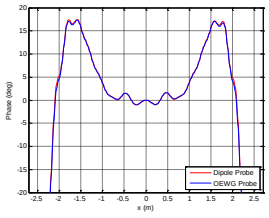


Fig. 13. Horizontal phase cut using dipole and OEWG field probe.

Figures 14 and 15 contain equivalent figures for the case where a SGH has been used as a pyramidal horn probe. Here it is evident from inspection of the amplitude and phase results that the high spatial frequency information within the QZ plots has been attenuated with the larger aperture effectively averaging out the measured response and thereby reducing the observed amplitude and peak-to-peak phase ripple. This is further confirmed by the circa 15 dB increase in the EMPL level between dipole probe and horn probe. Although not shown due to lack of space, equivalent results for the vertical cut exhibited similar phenomena. This probe dependent QZ is a well-known measurement effect but for the first time it has been possible to bound the SGH upper-bound measurement uncertainty and to provide tools necessary for verifying the appropriate choice of field probes.

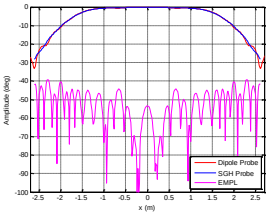


Fig. 14. Horizontal amplitude cut using dipole and SGH probe.

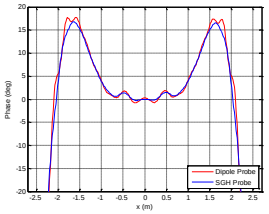


Fig. 15. Horizontal phase cut using dipole and SGH probe.

## IV. CONCLUSION

The construction of a complete end-to-end CEM model of a CATR including CATR QZ probing has enabled the validity of standard CATR probing techniques to be objectively and quantitatively examined. Here, it was found that the standard practice of employing a pyramidal horn, e.g., a SGH, as a field probe increases EMPL by *circa* 15 db by reducing peak-to-peak ripple across the probed QZ. This works also confirmed that an electrically small OEWG probe provides highly accurate measure of the QZ fields with an EMPL < -60 dB and in nearly all the range <-70 dB. As this paper details ongoing research, the planned future work is to include obtaining additional verification of the modeling technique using the alternative plane-wave spectrum scattering matrix representation of antenna-to-antenna coupling.

## REFERENCES

[1] C. G. Parini, R. Dubrovka, and S. F. Gregson, "CATR quiet zone modelling and the prediction of "measured" radiation pattern errors: comparison using a variety of electromagnetic simulation methods," *AMTA*, October 2015.

[2] C. G. Parini, R. Dubrovka, and S. F. Gregson, "Compact range quiet zone modelling: quantitative assessment using a variety of electromagnetic simulation methods," *LAPC*, November 2015.

[3] G. E. Hindman and D. Slater, "Anechoic chamber diagnostic imaging," *AMTA Symposium*, 1992.

[4] S. F. Gregson, C. G. Parini, and J. McCormick, *Principles of Planar Near-Field Antenna Measurements*, IET Press, 2007.

[5] P. N. Betjes, "An algorithm for automated phase center determination and its implementation," *AMTA Symposium*, 2007.

[6] C. G. Parini, S. F. Gregson, J. McCormick, and D. Janse van Rensburg, *Theory and Practice of Modern Antenna Range Measurements*, IET Press, 2014.

[7] M. Philippakis and C. G. Parini, "Compact antenna range performance evaluation using simulated pattern measurements," *IEE Proceedings Microwaves, Antennas and Propagation*, vol. 143, iss. 3, pp. 200-206, 1996, DOI: 10.1049/ip-map:19960398

[8] C. G. Parini and M. Philippakis, "The use of quiet zone prediction in the design of compact antenna test ranges," *IEE Proc., Microwave Antennas Propagation*, vol. 143, no. 3, pp. 193-199, 1996.

[9] C. Cappellin, S. Busk Sørensen, M. Paquay, and A. Østergaard, "An accurate and efficient error predictor tool for CATR measurements," 4th EuCAP 2010, Barcelona, 12-16 April 2010.

# Enhanced Artificial Immune System Algorithm and Its Comparison to Bio-Inspired Optimization Techniques for Electromagnetics Applications

**Ozlem Kilic and Quang M. Nguyen**

Department of Electrical Engineering and Computer Science
The Catholic University of America, Washington, DC, 20064, USA
kilic@cua.edu, 93nguyen@cardinalmail.cua.edu

***Abstract*** — This paper introduces an enhanced artificial immune system algorithm (EAIS) that benefits from a hybrid approach by integrating concepts from the genetic algorithm (GA) and particle swarm optimization (PSO). The potential of the EAIS algorithm is demonstrated by comparing its performance with other bio-inspired optimization algorithms; namely the particle swarm optimization (PSO) and the conventional artificial immune system (AIS) when applied to two electromagnetics applications, such as the design of antireflective surfaces, and microstrip electromagnetic band gap (EBG) structures.

***Index Terms*** — Antireflective surface, artificial immune system (AIS), bio-inspired optimization, enhanced artificial immune system (EAIS), microstrip (EBG), particle swarm optimization (PSO).

## I. INTRODUCTION

Bio-inspired optimization techniques typically rely on a number of agents that simultaneously sample the optimization space in a random fashion. The process is iterated until a desired solution or the maximum number of iterations is reached. The initial step is purely random, hence requires no a-priori guess of the solution. More intelligence is added to the heuristic search at each iteration by taking advantage of the accumulated knowledge of the search domain among the agents. This intelligence is based on the computation of a cost function, which is a measure of how well each agent has performed with respect to the desired state; with high costs referring to poor solutions. The basic principles of bio-inspired optimization methods are shown in Fig. 1.

The application of bio-inspired optimization techniques to engineering problems is not a new concept. One of the well-known and original algorithms of this nature is the genetic algorithm (GA), which is based on the genetic recombination and mutation of species, [1]. Some other bio-inspired optimization techniques include the particle swarm optimization (PSO), which is inspired by the intelligent search of bees in a swarm to find the best food source in a field, [2], and the artificial immune system (AIS), which is based on the behavior of our immune system in defending our body against viruses by adapting to the optimal antibody for a given antigen, [3]. Another recent bio-inspired algorithm is the covariance matrix adaption evolutionary strategy, which was applied to the design of linear arrays in [4]. Among these methods, GA and PSO have been applied to electromagnetics problems before. However, the application of AIS in electromagnetics have been relatively scarce. Most uses for these algorithms have been in the area of networks, resource constructed scheduling, data mining, etc. [5]. Our group has investigated AIS in the context of radar absorbing material design, and multi-beam satellite antenna side lobe control in [6]. In this paper, we further enhance the AIS algorithm (EAIS) and compare its performance to the conventional AIS and PSO for antireflective surfaces, and microstrip electromagnetic band gap (EBG) structures. We show that the consistent success of the enhanced AIS algorithm makes it a promising tool for the electromagnetics community.

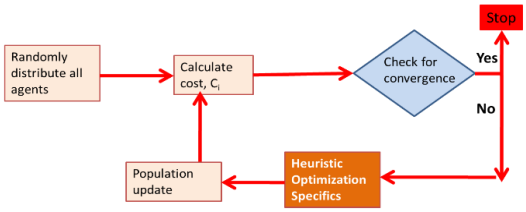


Fig. 1. A general block diagram of bio-inspired optimization methods.

The rest of the paper is organized as follows. Section 2 describes the principles of EAIS. Section 3 investigates the performance of AIS, PSO and EAIS when they are applied to electromagnetics designs. Finally, Section 4 concludes the paper.

## II. ENHANCED ARTIFICIAL IMMUNE SYSTEM ALGORITHM (EAIS)

The conventional AIS optimization is based on the clonal selection principles of our immune system

*Submitted On: November 6, 2015*
*Accepted On: March 10, 2016*

response to potential disease generating metabolisms, and simulates human body's defense system against viruses. Our adaptive immune system produces antibodies whose purpose is to bind to any antigen that it recognizes. For engineering applications, antibodies represent a possible solution to the optimization problem. The optimization space is discretized in order to emulate the binary form of gene behavior. The generic "Heuristic Optimization Specifics" step shown in Fig. 1 is replaced by four steps in AIS: cloning, mutation, combination and sorting as shown in Fig. 2.

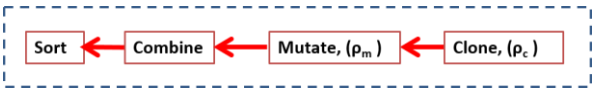


Fig. 2. Conventional AIS procedure steps.

In challenging problems, AIS can reach a state of stagnation where all good solutions in the set may differ by only a few bits [6]. In this paper, we incorporated modifications to the conventional AIS algorithm to improve its performance by bringing more intelligence to the mutation stage as well as by introducing concepts from other evolutionary algorithms. The EAIS specific procedures are shown in Fig. 3, where the dark shaded boxes indicate new steps to the process, and the light shade for the mutation step indicates a modification.


Fig. 3. Enhanced AIS procedure steps.

We modify the heuristic optimization specifics in AIS by modifying the mutation concept, and introducing a cross over operation. We also revise the population update process. The mutation stage benefits from the velocity and position update mechanism of PSO. The new cross over stage enhances the randomness using concepts from GA. Finally the population update stage utilizes PSO's global memory principles. The details of each enhancement stage are provided as follows.

*(i) Mutation Stage Enhancements*

Mutation enables AIS to randomly explore the search space by allowing it to move out of a local optimum and avoid stagnation. The conventional AIS algorithm carries this out by randomly flipping a certain number of bits in the solution set. The only intelligence incorporated in the conventional AIS at this stage is the number of bits to be flipped, with good solutions going through fewer flips than poor solutions. The proposed enhancement introduces a process similar to the velocity update mechanism of the PSO, where the bees get pulled towards the global best value. The value of the new antibody $Ab^*$ after the mutation process is computed as in Equation (1):

$$Ab^* = Ab + \alpha \times rand \times Ab + \alpha \times rand \times (Ab - Ab_{best}), \quad (1)$$

where $Ab_{best}$ is the value of the best solution in the set, $Ab$ is the value before mutation, and $\alpha$ is the mutation rate which exponentially varies as a function of the rank of the antibody, i.e., $\alpha = e^{-1/k}$ and *rand* is a random number between [0-1]. This process influences the mutation towards the best solution in the set, [7].

*(ii) Crossover Stage Enhancements*

Crossover is a process where a new binary set is produced from the existing set by randomly combining portions from different solutions. It is used in GA to create "children" from "a parent." This concept is applied to EAIS to create a new set of antibodies by crossing the antibodies created as a result of the cloning and mutation stages. The modified algorithm selects the top $N_\beta$ antibodies from the output of the conventional AIS, i.e., the combined set of cloning and mutation operations. Each antibody is split into 2 segments. The number of bits in each segments is defined by the user, based on the cross-over split ratio $n_1 : n_2$ where $n_1$ denotes the number of bits with the most significant bits in the string, and $n_2$ denotes the number of remaining bits. The two segments are randomly crossed among each other to create a new set of $N_x$ antibodies, where $N_x = \rho_x \times N_a$ is the size of the cross-over set, and $\rho_x$ is the cross over ratio. The concept of crossover is demonstrated in Fig. 4. Finally, the crossover set is combined with the cloned and mutated sets. The antibodies are sorted one more time with respect to their cost values. The top $N_a$ antibodies are selected from this set to start over again.

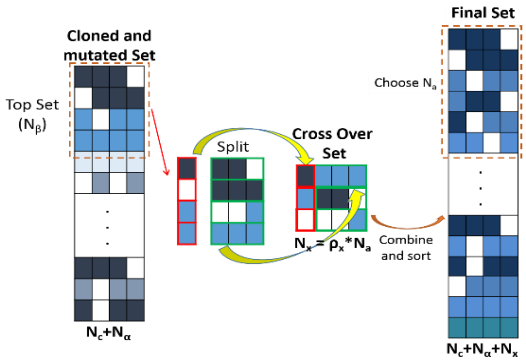


Fig. 4. Crossover concept of EAIS.

*(iii) Population Update Stage Enhancements*

At this point, the original population has been replaced with the new set of $(N_a)$ antibodies utilizing cloning, mutation and cross over. The AIS algorithm can

continue to iterate these steps to search for the solution. In challenging problems, AIS can reach a state of stagnation where all good solutions in the set may differ by only a few bits. Another enhancement inspired by PSO is implemented at this stage. The solution set of $N_a$ antibodies is split into three sets for separate treatments. The top few solutions from Set 1 are kept in order to remember the best solutions achieved. This is similar to the group memory concept in PSO in the context of the global best term. The rest of the antibodies are divided into two groups, i.e., Sets 2 and 3. Antibodies in Set 2 are replaced by a local random search in the vicinity of the best solution. Set 3 is replaced by a global search carried out randomly in the entire optimization space. The range of the local search can be adjusted dynamically to focus more in the vicinity of the best solutions as the number of iterations increase. The concept of these three sets and how they are treated are shown in Fig. 5. For the local search in Set 2, the approach is to utilize PSO with only a few agents and for a few iterations. The remaining solutions in Set 3 are simply replaced randomly. It should be noted that the cost function computation time is the dominant term for these random search optimization algorithms. Thus, for an equivalent problem; i.e., the same number of cost function calls per iteration, EAIS computation time is similar to AIS regardless of the few extra steps added.

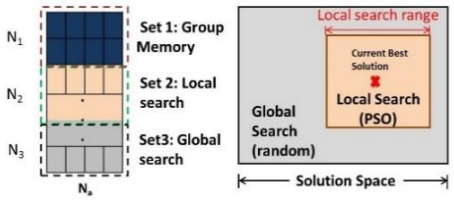


Fig. 5. Population update process of EAIS.

## III. APPLICATION TO ELECTROMAGNETIC PROBLEMS

### A. Antireflective Surface (AR) design

The first application we consider addresses an anti-reflective surface design, which is useful for both military (e.g., camouflaging) and commercial applications (e.g., efficient collection of energy such as in microwave or millimeter wave lenses). The design is inspired by the moth-eye structure, which consists of multiple layers of periodic gratings that enable the absorption of light at a wide range of incidence angles, [8]. In our application, we use a dielectric slab with an inverse moth eye pattern (i.e., holes rather than protrusions) applied to both top and bottom surfaces of the structure. We use the rigorous coupled wave algorithm (RCW) to simulate the model. Our goal is to achieve a desired total reflection coefficient of $\Gamma \le -30\,dB$ within the Ka-band over the 32-38 GHz bandwidth.

The design has an infinitely thick (i.e., half space) substrate with a dielectric constant of $\varepsilon_r = 2.56$, and an index of refraction of $n_s = 1.6$. The holes are backfilled with air, $n_h = 1$ and the grating period, $\Lambda$, is fixed at 3.1 mm, as depicted in Fig. 6. The grating heights, $h_1$ and $h_2$, and the hole diameters, $d_1$ and $d_2$, are the variables of the design. The incident field is assumed to be a TE polarized plane wave obliquely incident on the surface. The cost function of EAIS is defined as the square of a difference between the desired criteria and the reflection coefficient. The parameters of the optimization algorithms are summarized in Table 1.

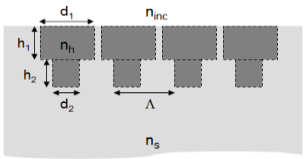


Fig. 6. Inverse half space AR surface design.

Table 1: Algorithm parameters for AR surface design

| | PSO | AIS | EAIS |
|---|---|---|---|
| | $c_1 = c_2 = 1$ | $\rho_c = 0.6$<br>$\rho_m = 0.5$ | $\rho_c = 0.6,\ \rho_x = 1$<br>$n_1 / n_2 = 0.2$ |
| $N_a$ | 96 | 28 | 18 |
| $N_b$ | n/a | 12 | 12 |

The bandwidth was sampled in steps of 1 GHz. The best solution achieved at the end of 100 iterations is shown in Table 2 along with the best minimum reflection coefficients over the 32-38 GHz bandwidth. The optimized reflection coefficients is plotted in Fig. 7 (a) as a function of the incidence angle at the center frequency, i.e., f = 35 GHz for the three algorithms. We observe that for this particular angle, AIS does not converge at $\theta=40^0$. Also, overall it is evident that PSO has reached a better solution for a wide range of incident angles. However, it should be noted that achieving a value better than the desired criteria, i.e., $\Gamma \le -30\,dB$, is not part of the objectives for any of these algorithms, i.e., each algorithm accepts any value of $\Gamma \le -30\,dB$ as a converged solution. From the perspective of the rate of convergence, EAIS performs the best as shown in Fig. 7 (b), where $\Gamma$ is plotted against the number of iterations.

Table 2: AR surface design solution

| AR Design | PSO | AIS | EAIS |
|---|---|---|---|
| $h_1$ (mm) | 2.58 | 2.67 | 2.60 |
| $h_2$ (mm) | 1.82 | 1.74 | 1.80 |
| $d_1$ (mm) | 3.02 | 3.01 | 3.02 |
| $d_2$ (mm) | 2.15 | 2.09 | 2.15 |
| $\Gamma$ (dB) | -28.62 | -28.52 | -28.62 |

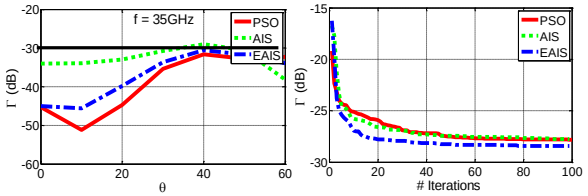


(a) (b)

Fig. 7. Optimized AR surface design at f = 35 GHz and performance of three algorithms.

### B. Microstrip EBG structures

In this application, we design a low pass filter operating at [4-7.5 GHz] such that $S_{21} \geq$ -5 dB across [4-6 GHz], and $S_{21} \leq$ -25 dB over [6.5-7.5 GHz]. To achieve the performance, we consider a 50 Ohm microstrip line symmetrically residing on a periodically etched ground plane, where 50 mil thick, 2.33x1.53 inches RT/Duroid 6010 ( $\varepsilon_r = 10.2$ ) is used as the substrate. To model the structure, we use EM commercial software, FEKO, which is based on the Method of Moments (MoM).

The simulated model for our design is shown in Fig. 8. The optimization variables; i.e., $D_1$ and $D_2$ are set to be between 50-250 mils. The optimization parameters used for each algorithm are summarized in Table 3. The solution achieved by each algorithm is summarized in Table 4, and the achieved performance is plotted in Fig. 9. We observe that, all three algorithms converge to similar solutions. A plot of the best cost versus the number of iterations is shown Fig. 9 (b). Although EAIS reaches the vicinity of the desired solution fastest, PSO achieves the best cost in the end.

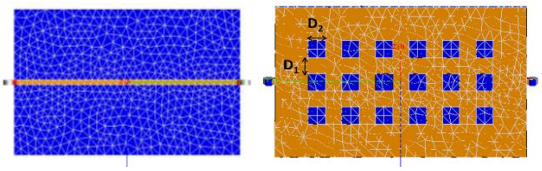


(a) Top view (b) Bottom view

Fig. 8. Microstrip EBG line with etched squares in the ground plane.

Table 3: Algorithm parameters for microstrip EBG

| | PSO | AIS | EAIS |
|---|---|---|---|
| $N_a$ | 10 | 4 | 2 |
| $N_b$ | n/a | 12 | 12 |
| # Cost computations/iteration | 10 | 10 | 10 |
| $N_{max}$ | 14 | 14 | 14 |

Table 4: Microstrip EBG design solution

| | PSO | AIS | EAIS |
|---|---|---|---|
| $D_1$ (mil) | 50 | 55 | 58 |
| $D_2$ (mil) | 222 | 216 | 213 |

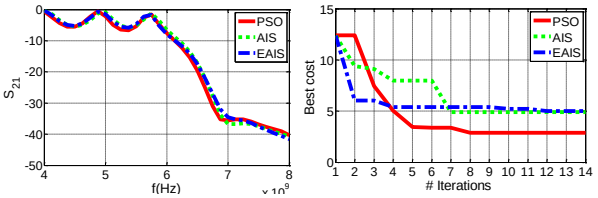


(a) (b)

Fig. 9. Optimized microstrip EBG structure and performance of three algorithms.

## IV. CONCLUSION

The robustness of the EAIS algorithm was demonstrated in comparison to PSO and AIS as they were applied to two electromagnetics applications; antireflective surface design using RCW, and microstrip electromagnetic band gap structure using MoM. EAIS consistently performed more robust than the other two algorithms. While it can never be claimed that a particular random search algorithm will always perform better than others, as the nature of a problem might fit the principles of an algorithm better at times, EAIS was shown to be consistently robust presenting itself as a viable tool for challenging electromagnetics problems.

## REFERENCES

[1] R. L. Haupt, "An introduction to genetic algorithms for electromagnetics," *IEEE Antennas Propagat. Mag.*, vol. 37, pp.7-15, 1995.

[2] J. Kennedy and R. Eberhart, "Particle swarm optimization," *Proc. IEEE Int. Conf. Neural Networks*, vol. 4, pp. 1942-1948, 1995.

[3] L. N. De Castro and F. J. Von Zuben, "Learning and optimization using the clonal selection principle," *IEEE Trans. Evol. Comput.*, vol. 6, pp. 239-251, 2002.

[4] M. D. Gregory and D. H. Werner, "Design of high performance compact linear ultra-wideband arrays with the CMA evolutionary strategy," *IEEE Int'l Symp. on Ant. and Propag.*, Toronto, ON, 2010.

[5] R. S. Parpinelli, H. S. Lopes, and A. A. Freitas, "Data mining with an ant colony optimization algorithm," *IEEE Trans. Evol. Comp.*, vol. 6, iss. 4, pp. 321-332.

[6] O. Kilic and Q. Nguyen, "Application of artificial immune system algorithm to electromagnetics problems," *PIER B*, vol. 20, pp. 1-17, 2010.

[7] S. A. P. Ramaswamy, G. K. Venayagamoorthy, and S. N. Balakrishnan, "Optimal control of class of non-linear plants using artificial immune systems: application of the clonal selection algorithm," *22nd IEEE Int'l Symp. on Intelligent Control*, pp. 249-254, 1-3 Oct. 2007.

[8] M. S. Mirotznik, B. L. Good, P. Ransom, D. Wikner, and J. N. Mait, "Broadband antireflective properties of inverse Motheye surfaces," *IEEE Trans. Antennas Propagat.*, AP-58, 9, pp. 2969-2980, Sep. 2010.

# Experimental Benchmarking of Unstructured Transmission Line Modelling (UTLM) Method in Modelling Twisted Wires

**Xuesong Meng*, Phillip Sewell, Nur H. A. Rahman, Ana Vukovic, and Trevor M. Benson**

George Green Institute for Electromagnetics Research
University of Nottingham, Nottingham, NG7 2RD, UK
*xuesong.meng@nottingham.ac.uk

***Abstract*** ─ In this paper the Unstructured Transmission Line Modelling (UTLM) method based on a tetrahedral mesh has been applied to modelling of the coupling between a single wire and a twisted wire pair. The effects of wire twisting on the crosstalk and coupling between wires are modelled by explicitly meshing wire geometries; simulation results are compared with experimental ones. Excellent agreement between simulated and measured results validates the viability and accuracy of the UTLM method and indicates the potential of the UTLM method for modelling complex wire structures.

***Index Terms*** ─ Crosstalk, experimental benchmarking, Transmission Line Modelling (TLM) method, twisted wires, twisting effects, Unstructured Transmission Line Modelling (UTLM) method.

## I. INTRODUCTION

Wires and cables play an important role in modern electronic systems, especially in the aerospace and automotive industries. They transmit signals between pieces of equipment and at the same time couple with the ambient electromagnetic fields. The electromagnetic interference (EMI) between wires and cables may affect the normal operation of equipment. It is therefore important to develop efficient and versatile methodologies that can predict the coupling strength between wires and cables.

The Unstructured Transmission Line Modelling (UTLM) method, fully presented and validated in [1-2], is a Transmission Line Modelling (TLM) method based on tetrahedral meshes [3]. Whilst the use of a TLM method based on structured cuboidal meshes has been widely reported, especially for Electromagnetic Compatibility (EMC) studies and microwave modelling, the advantages and characteristics of the UTLM method have not as yet been fully explored for such a variety of applications. For instance, when modelling curved structures, a very fine mesh is needed for the cuboidal mesh based TLM method to approximate the curved boundaries. This not only leads to large computational resources, even when using Octree sub-division technique [4], but also leads to stair-stepping problems [5]. Furthermore, its accuracy in representing the curved boundaries is piece-wise constant. In contrast, the UTLM method can better describe arbitrary shaped geometries, especially those involving curved structures, with no stair-stepping approximations and with a piece-wise-linear accuracy. One key feature of UTLM is the wide dynamic range of cell sizes that can be used. Importantly, a clustering technique whereby clusters of very small cells are grouped into larger cell entities for which the scattering is done implicitly, has been integrated into the UTLM method to allow a practical small time step to be used in a simulation [6]. These characteristics make the UTLM method a very good candidate to model in detail the coupling between wires and cables, a feature which is especially important within an aerospace context.

Some initial experimental benchmarking of a UTLM model explicitly meshing wires has been presented in [7], where the UTLM method was applied to the simulation of a canonical two parallel wire coupling problem. The paper discussed that small wire diameters lead to large computational costs in a discretized numerical simulation. Although an embedded thin wire model [8] has been widely adopted to reduce computational costs, it has difficulties in dealing with twisted wires, especially when other structures are in close proximity to the wire geometries. The purpose of this paper is to demonstrate how the wide dynamic range of cell sizes within ULTM enables the modelling of the coupling between a single wire and a twisted wire pair by explicitly meshing them, and to validate the approach by comparison with experiments. In the scenario considered the single wire is used for excitation and the twisted wire pair is used as victim on which crosstalk is observed. The crosstalk between wires is analyzed for different wire terminations, and both with and without twisting of the wire pair. The simulated results are compared with measurements. The paper is organized as follows: in the next section the experimental set up is described, followed by a description of the simulated model. Section IV outlines the comparison of the crosstalk between simulated and measured results and

*Submitted On: December 16, 2015*
*Accepted On: May 16, 2016*

Section V summarizes the main conclusions of the paper.

## II. PROBLEM DESCRIPTION

In this section, the experimental setup used to study the twisting effects on coupling between wires is described.

In order to consider the twisting effects, a single core copper wire is excited as the source and a twisted wire pair is used as the victim. The single core wire has a radius of $r_w$ = 0.04 cm. The separations between ports are *s1* = 2 cm and *s2* = 1 cm. The wires are placed near a L shape ground plane as shown in Fig. 1 (a) and mounted on to the two metal bulkheads using SMA bulkhead connectors as shown in Fig. 1 (b). The wires are situated above the bottom ground plane by a height, $h$ = 8 cm. The distance between port 1 and the left ground plane is $d$ = 12.5 cm as shown in Fig.1 (a). The length of the wires is $L$ = 100 cm. The twisted wire pair has 20 twists along its length. The metal bulkheads each have dimensions of 30 cm × 30 cm.

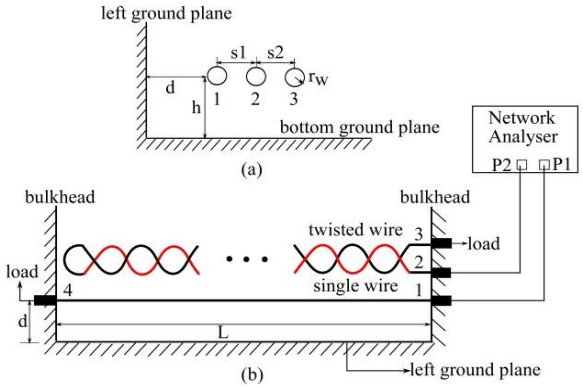


Fig. 1. (a) A single wire and a twisted wire pair are near the L shape ground plane; (b) the top view of the setup.

In the experiment, the twisted wire pair is made by folding a single core copper wire of length *2L* and twisting the two halves to create the configuration shown in Fig. 1 (b). At the right end, one wire of the twisted wire pair is connected to port 2 and the other one is connected to port 3. Port 1 is connected to the right end of the single wire as an excitation. Measurements are made on port 2 using a Network Analyzer (Agilent E5062A). Port 3 and port 4 (the left end of the single wire) are connected to a load, which could be a 50 ohms load, a short circuit or an open circuit.

## III. NUMERICAL MODEL

The problem defined in Section II is described for numerical modelling purposes using University of Nottingham (UoN) in-house geometry software that provides a triangulated surface representation of the structure. The single wire is built as a metal cylinder. Both ends of the single wire are connected to the cores of two coaxial probes, respectively. One of them is modelled as port 1 in Fig.1 (b) to excite the fundamental TEM mode and the other one is modelled as port 4 to terminate the wire.

The twisted wire pair is built by twisting two metal cylinders using a bifilar helix model. The circular cross-section of each wire is discretized by a $N_1$-sided polygon (where $N_1$ is an integer number). Each wire is then represented by $N_2$ piecewise linear segments ($N_2$ is also an integer number) that follow a helical path rotating around the axis of the twisted wires in such a manner that each wire's cross section remains perpendicular to its own axis. Figure 2 shows one example of a two wire twisted pair built with the UoN in-house geometry software.

Fig. 2. The geometrical model for a two wire twisted pair.

At one end of the twisted wire pair, the wires are connected using a metal cylinder. The wires follow a curved route defined by a Bezier curve. At the other end, the two wires are connected to the cores of two coaxial probes, respectively. One of the coaxial probes is modelled as port 2 in Fig. 1 (b) to observe the coupling to the TEM mode of the twisted wire pair; the other one is modelled as port 3 in Fig. 1 (b) to terminate the wire.

The structure is meshed using our UoN in-house Delaunay Mesher software as a hybrid tetrahedral-cubic mesh. The meshed structure is shown in Fig. 3.

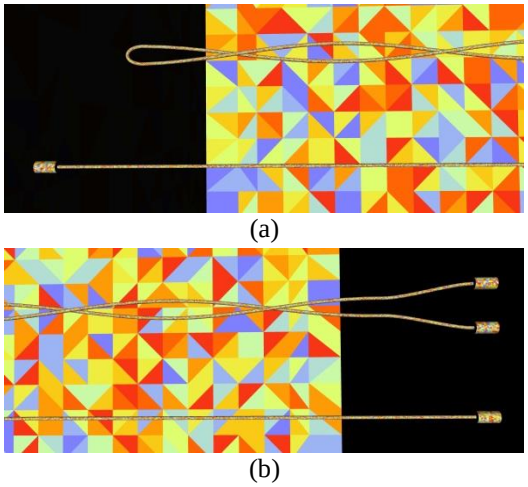


Fig. 3. The meshed geometry showing the triangulated interfaces between different materials: (a) left end of the structure and (b) the right end of the structure with a mesh size of 1 cm. Randomized colouring is used to show the triangle sizes and shapes.

Figures 3 (a) and (b) show the left and right ends of the structure as in Fig. 1 (b), respectively. The wires are meshed using a tetrahedral mesh, which is better able to describe curved structures, and the surrounding environment is meshed using a cuboidal mesh with a mesh size of 1 cm. Although the mesh is very small around the wires, the cell clustering enabled a time step of 0.08 ps to be used in the simulation [6]. The total number of time steps is 2,000,000. The success of meshing twisted wires with such small diameters indicates the great potential of the UTLM method in dealing with complex wire structures.

## IV. CROSSTALK BETWEEN WIRES

In this section, the twisting effects on the coupling between wires are discussed for different termination conditions, using the UTLM simulation and experimental measurements.

The crosstalk between wires is described using the $S_{21}$ parameter. In order to account for the influence of the twisting of the wires, the crosstalk between the single wire and a pair of parallel wires is also simulated and measured.

Figure 4 compares the UTLM simulation and experiment results for the crosstalk between the excitation single wire and the pair of twisted wires and the crosstalk between the single wire and the pair of parallel wires for different port 3 and 4 terminations, namely, (a) a short circuit, (b) a 50 ohms load and (c) an open circuit. The UTLM simulation results show very good agreement with those from experiment for all three terminations, so validating the accuracy of the UTLM simulations including the twisted wires.

The twisting effects on the coupling between wires can also be observed from Fig. 4. For short circuit and 50 ohms load terminations, the coupling between wires is reduced greatly in the relatively low frequencies. For example, at 1 MHz, a 20 dB crosstalk reduction for short circuit termination and a 17 dB crosstalk reduction for a 50 ohms load termination are observed in Figs. 4 (a) and (b). As the frequency increases, the crosstalk reduction becomes smaller. For open circuit termination, the twisting does not have any significant effect on the coupling between wires.

The twisting effects on the coupling between wires can be explained as follows. In the relatively low frequencies, the coupling between wires is the combination of inductive coupling and capacitive coupling as shown in [9]. Twisting the wires mainly reduces the inductive coupling, while it has no effect on the capacitive coupling. For low impedance terminations, the inductive coupling dominates the capacitive coupling, so the twisting reduces the total coupling; for high impedance terminations, the capacitive coupling dominates the inductive coupling, so the twisting has no significant effect on the total coupling.

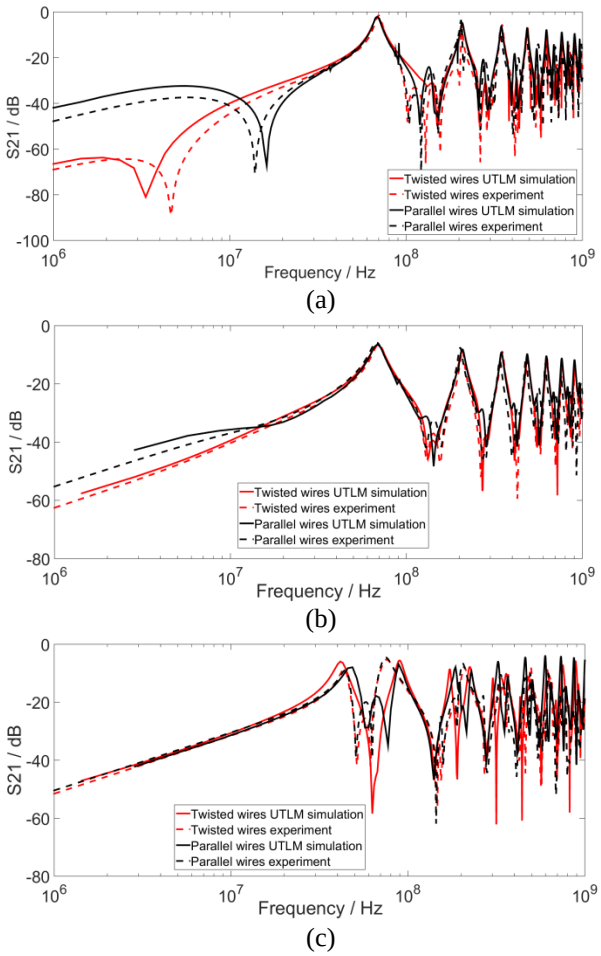


Fig. 4. Comparison of the UTLM simulation and experiment results for the crosstalk between the single wire and the pair of twisted wires and between the single wire and the pair of parallel wires, when ports 3 and 4 are terminated with: (a) a short circuit, (b) a 50 ohms load, and (c) an open circuit.

It is also noted that in Fig. 4 (a), for short circuit termination, there is a big discrepancy in the frequency at which the first dip in the crosstalk between the single wire and the twisted wire pair occurs. This can be explained since, for very low impedance (short circuit), the crosstalk at relatively low frequencies is very sensitive to the twist [9]. Even a very small non-uniformity in the twist could lead to a big change in the crosstalk. In the experiment, although every effort was made to make the twist uniform along the length, it was still unlikely to be a perfectly uniform twist. In the simulation it is quite easy to incorporate a perfect twist. To explore this further, two experiments have been undertaken, in which twisted wire pairs were made from two identical wires with a twist rate of 20 twists/m. The $S_{21}$ parameters measured for each case are shown in Fig. 5. It is seen that the two results agree well with each other

for the relatively high frequencies but not for the relatively low frequencies. The frequency at which the first dip in $S_{21}$ occurs in each experiment is different. The same experiments were also conducted for the 50 ohms load and open circuit terminations; in both these cases, the two sets of experimental results agree very well with each other. In conclusion, it is impossible to precisely predict the coupling between the single wire and the twisted wire pair at very low termination impedance at relatively low frequencies because of the sensitivity to the exact twist. Nevertheless, the UTLM simulation is able to predict the coupling for very low termination impedance at relatively high frequencies and for low and high termination impedances over the whole frequency range, very well.

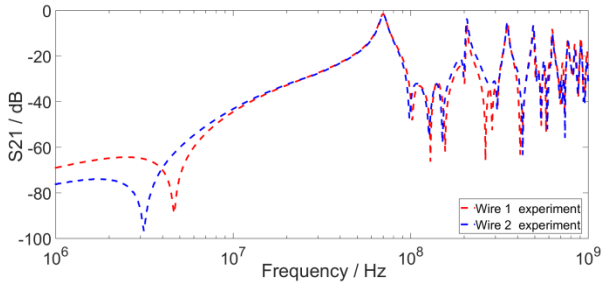


Fig. 5. The coupling between the single wire and the twisted wire pair with a short circuit termination; results from different experiments.

## V. CONCLUSION

The Unstructured Transmission Line Modelling (UTLM) method has been successfully applied to model the coupling between a single wire and a pair of twisted wires by explicitly meshing the complete wire geometry. This is enabled by the wide dynamic range of mesh size that can be used within UTLM. The method shows powerful capability in meshing wires with small diameters within a large space. The accuracy of the UTLM method for this class of problems has been validated for the first time by comparing the simulated results for coupling between wires with experimental ones. The close agreement between the simulated and experimental results confirms that the UTLM method is a very useful and powerful tool that can be used for modelling complex wire structures.

## ACKNOWLEDGMENT

The work outlined above was carried out as part of ICE-NITE (see http://www.liv.ac.uk/icenite/), a collaborative research project supported by Innovate UK under contract reference 101665. The project consortium includes BAE SYSTEMS Limited (coordinator), Bombardier, Horiba MIRA Limited, ITI Limited, The University of Liverpool, and The University of Nottingham.

The authors wish to thank Prof. C. Jones and Dr. S. Earl of BAE SYSTEMS for valuable discussions.

## REFERENCES

[1] P. Sewell, J. Wykes, T. Benson, C. Christopoulos, D. Thomas, and A. Vukovic, "Transmission-line modeling using unstructured triangular meshes," *IEEE Trans. on Microwave Theory and Techniques*, vol. 52, no. 5, pp. 1490-1497, 2004.

[2] P. Sewell, T. M. Benson, C. Christopoulos, D. W. P. Thomas, A. Vukovic, and J. G. Wykes, "Transmission line modeling (TLM) based upon unstructured tetrahedral meshes," *IEEE Trans. on Microwave Theory and Techniques*, vol. 53, pp. 1919-1928, 2005.

[3] C. Christopoulos, *The Transmission-Line Modeling Method TLM*. New York: IEEE Press, 1995.

[4] P. S. Duxbury, J. Wlodarczyk, and R. A. Scaramuzza, "The implementation and benefits of Octree staggered meshing in a TLM based EM simulation package," *2004 RF and Microwave Conference*, 2004.

[5] A. Cangellaris and D. Wright, "Analysis of the numerical error caused by the stair-stepped approximation of a conducting boundary in FDTD simulations of electromagnetic phenomena," *IEEE Trans. on Microwave Theory and Techniques*, vol. 39, pp. 1518-1525, 1991.

[6] P. Sewell, T. Benson, C. Christopoulos, D. Thomas, A. Vukovic, and J. Wykes, "Implicit element clustering for tetrahedral transmission line modeling (TLM)," *IEEE Trans. on Microwave Theory and Techniques*, vol. 57, no. 8, pp. 2005-2014, 2009.

[7] X. Meng, P. Sewell, A. Vukovic, Z. Zhang, and T. Benson, "Experimental benchmarking of unstructured transmission line modelling method (UTLM) simulations of explicitly meshed wiring," in *Computational Electromagnetics International Workshop (CEM) 2015*, pp. 1-2, 2015.

[8] P. Sewell, Y. K. Choong, and C. Christopoulos, "An accurate thin-wire model for 3-D TLM simulations," *IEEE Trans. on Electromagnetic Compatibility*, vol. 45, no. 2, pp. 207-217, 2003.

[9] C. R. Paul and M. B. Jolly, "Sensitivity of crosstalk in twisted-pair circuits to line twist," *IEEE Trans. on Electromagnetic Compatibility*, vol. 24, no. 3, pp. 359-364, 1982.

# Four-Stage Split-Step 2D FDTD Method with Error-Cancellation Features

**Theodoros T. Zygiridis [1], Nikolaos V. Kantartzis [2], and Theodoros D. Tsiboukis [2]**

[1] Department of Informatics and Telecommunications Engineering
University of Western Macedonia, Kozani, 50100, Greece
tzygiridis@uowm.gr

[2] Department of Electrical and Computer Engineering
Aristotle University of Thessaloniki, Thessaloniki, 54124, Greece
kant@auth.gr, tsibukis@auth.gr

***Abstract*** ─ We develop a methodology that enables the proper introduction of high-order spatial operators in an unconditionally-stable, split-step, finite-difference time-domain scheme. The proposed approach yields spatial approximations that guarantee better balancing of space-time errors, compared to standard fourth-order expressions. The latter are not as efficient as expected, due to their unmatched order with the scheme's second-order temporal accuracy. Our technique treats the dispersion relation as an error descriptor, derives spatial formulae that change with the cell shape and time-step size, and rectifies the performance over all frequencies.

***Index Terms*** ─ Finite-difference time-domain (FDTD) methods, numerical-dispersion relation, split-step approaches, unconditionally-stable methods.

## I. INTRODUCTION

Among the diverse advances of Yee's finite-difference time-domain (FDTD) method [1,2], approaches featuring unconditional stability [3] belong to the most significant contributions. Numerical schemes such as the alternating-direction implicit [4] and the locally one-dimensional FDTD techniques [5] are free from constraints governing their temporal sampling density, which is an advantageous property in many electromagnetic simulations. Other solutions based on split-step procedures [6-8] also exhibit similar behavior, and have been the subject of various studies [9,10].

In the context of the aforementioned implicit methods, the improvement of temporal accuracy can be a computationally expensive task, as it commonly requires the increase of the intermediate stages for the successive update of field components. On the other hand, direct incorporation of high-order spatial operators is a simpler and more straightforward approach towards performance upgrade, although it too augments the algorithm's complexity. Since the combination of accurate spatial approximations with low (first or second) temporal order usually impedes the full exploitation of high-order operators' potential, amending techniques may be applied for further error mitigation. The implementation of constant-valued correctional coefficients, calculated in diverse ways, is a popular practice in this category of useful concepts [11,12].

This paper's purpose is to efficiently incorporate four-point spatial approximations into a two-dimensional (2D) four-stage split-step FDTD (SS-FDTD) method, aiming at a balanced treatment of space-time errors. Our approach exploits the scheme's dispersion relation to represent the inherent discretization errors. By using the estimator's Taylor polynomial, improvement over all frequencies is facilitated, while its trigonometric expansion leads to accuracy correction irrespective of propagation direction. The resulting unconditionally-stable algorithm performs better than its counterpart with standard high-order operators, verifying the optimal use of computational resources.

## II. MODIFIED 4-STAGE SS-FDTD METHOD

The considered SS-FDTD scheme has second-order temporal accuracy, and the time-stepping is performed according to the following splitting approach:

$$\begin{aligned}
\left([\mathbf{I}]-\tfrac{\Delta t}{4}[\mathbf{A}]\right)[\mathbf{u}]^{n+1/4} &= \left([\mathbf{I}]+\tfrac{\Delta t}{4}[\mathbf{A}]\right)[\mathbf{u}]^{n} \\
\left([\mathbf{I}]-\tfrac{\Delta t}{4}[\mathbf{B}]\right)[\mathbf{u}]^{n+1/2} &= \left([\mathbf{I}]+\tfrac{\Delta t}{4}[\mathbf{B}]\right)[\mathbf{u}]^{n+1/4} \\
\left([\mathbf{I}]-\tfrac{\Delta t}{4}[\mathbf{B}]\right)[\mathbf{u}]^{n+3/4} &= \left([\mathbf{I}]+\tfrac{\Delta t}{4}[\mathbf{B}]\right)[\mathbf{u}]^{n+1/2} \\
\left([\mathbf{I}]-\tfrac{\Delta t}{4}[\mathbf{A}]\right)[\mathbf{u}]^{n+1} &= \left([\mathbf{I}]+\tfrac{\Delta t}{4}[\mathbf{A}]\right)[\mathbf{u}]^{n+3/4}
\end{aligned}, \quad (1)$$

where $[\mathbf{I}]$ is the 3×3 unitary matrix, $[\mathbf{u}] = [E_x\ E_y\ H_z]^{\mathrm{T}}$ is the vector with the three field components in 2D, $\Delta t$ is the time increment, and $[\mathbf{A}]$,$[\mathbf{B}]$ are derivative matrices:

$$[\mathbf{A}] = \begin{bmatrix} 0 & 0 & \frac{1}{\varepsilon}D_y \\ 0 & 0 & 0 \\ \frac{1}{\mu}D_y & 0 & 0 \end{bmatrix},\ [\mathbf{B}] = -\begin{bmatrix} 0 & 0 & 0 \\ 0 & 0 & \frac{1}{\varepsilon}D_x \\ 0 & \frac{1}{\mu}D_x & 0 \end{bmatrix}. \quad (2)$$

In its conventional form [8], the methodology relies on

*Submitted On: December 31, 2015*
*Accepted On: April 19, 2016*

standard second-order approximations of the derivatives. Here, we adopt four-point symmetric expressions,

$$D_x u|_{i,j}^n = \frac{1}{\Delta x}\sum_{m=1}^{2} C_m^x \left( u|_{i+\frac{2m-1}{2},j}^n - u|_{i-\frac{2m-1}{2},j}^n \right), \quad (3)$$

$$D_y u|_{i,j}^n = \frac{1}{\Delta y}\sum_{m=1}^{2} C_m^y \left( u|_{i,j+\frac{2m-1}{2}}^n - u|_{i,j-\frac{2m-1}{2}}^n \right), \quad (4)$$

whose final form is determined via an analytical procedure that aims at suitable error cancellation.

The basic element of the proposed optimization approach is the scheme's numerical dispersion relation, and its utilization as a means to express the inherent dispersion errors. The dispersion relation is obtained after introducing plane-wave forms in (1),

$$[\mathbf{u}] = [\mathbf{u}_0] e^{\mathrm{j}(\omega t - \tilde{k}_x x - \tilde{k}_y y)}, \quad (5)$$

and requiring the existence of non-trivial solutions for the resulting system ($\tilde{k}_x = \tilde{k}\cos\theta$, $\tilde{k}_y = \tilde{k}\sin\theta$, $\tilde{k}$ is the numerical wavenumber). In essence, the condition,

$$\det\left( e^{\mathrm{j}\omega\Delta t}[\mathbf{I}] - [\mathbf{L}_{\mathcal{A}}][\mathbf{L}_{\mathcal{B}}]^2[\mathbf{L}_{\mathcal{A}}] \right) = 0, \quad (6)$$

is obtained, where

$$[\mathbf{L}_{\mathbf{U}}] = \left( [\mathbf{I}] - \tfrac{\Delta t}{4}[\mathbf{U}] \right)^{-1} \left( [\mathbf{I}] + \tfrac{\Delta t}{4}[\mathbf{U}] \right), \quad (7)$$

and matrices $[\boldsymbol{\mathcal{A}}]$, $[\boldsymbol{\mathcal{B}}]$ are derived from $[\mathbf{A}]$, $[\mathbf{B}]$, respectively, after replacing the $D_x$, $D_y$ operators with:

$$X = -\frac{2\mathrm{j}}{\Delta x}\sum_{m=1}^{2} C_m^x \sin\left( \tfrac{2m-1}{2}\tilde{k}_x \Delta x \right), \quad (8)$$

$$Y = -\frac{2\mathrm{j}}{\Delta y}\sum_{m=1}^{2} C_m^y \sin\left( \tfrac{2m-1}{2}\tilde{k}_y \Delta y \right). \quad (9)$$

The resulting dispersion equation has the form:

$$\cos(\omega\Delta t) = \frac{\alpha_{\mathrm{num}}(\tilde{k},\omega,\theta)}{\alpha_{\mathrm{den}}(\tilde{k},\omega,\theta)}, \quad (10)$$

where

$$\alpha_{\mathrm{num}} = \left(16 + c_0^2\Delta t^2 X^2\right)^2 \left(16 + c_0^2\Delta t^2 Y^2\right)^2 + 64 c_0^2\Delta t^2 \left(X^2 + Y^2\right)\left(256 + c_0^4\Delta t^2 X^2 Y^2\right), \quad (11)$$

$$\alpha_{\mathrm{den}} = \left(16 - c_0^2\Delta t^2 X^2\right)^2 \left(16 - c_0^2\Delta t^2 Y^2\right)^2. \quad (12)$$

Of crucial importance is the definition of the error formula that is used to represent the discretization flaws. As we are interested in combating the inaccuracies pertinent to the phase velocity, we define,

$$\Lambda(\omega,\theta) = \cos(\omega\Delta t) - \frac{\alpha_{\mathrm{num}}(k,\omega,\theta)}{\alpha_{\mathrm{den}}(k,\omega,\theta)}, \quad (13)$$

which practically describes the deviation from the numerical dispersion relation, once the numerical wavevector has been replaced by its exact value $k = \omega/c_0$. Now, the determination of the optimum spatial operators is reduced to the following problem: find suitable coefficients $C_1^x$, $C_2^x$, $C_1^y$, $C_2^y$, so that the magnitude of $\Lambda(\omega,\theta)$ is rendered as close to zero as possible, for all frequencies $\omega$ and propagation angles $\theta$.

In order to satisfy – to the best possible degree – the aforementioned requirements, the Taylor-series of (13) with respect to the spatial increment is exploited. Specifically, we are working on the expression:

$$\Lambda(\omega,\theta) = \delta^{(2)}(\theta)(k\Delta x)^2 + \delta^{(4)}(\theta)(k\Delta x)^4 + \ldots. \quad (14)$$

This expansion effectively isolates the dependences on frequency and propagation direction, which significantly facilitates their separate treatment. Specifically, accuracy improvement irrespective of frequency is now possible, by cancelling the corresponding $\delta$ coefficients, which do not depend on $\omega$. If it was possible to accomplish $\delta^{(2)} = \delta^{(4)} = \ldots = 0$, a totally error-free FDTD scheme would be devised. Apparently, this is an observation of merely theoretical interest, since the discretization error can be controlled only to a certain degree in practice. In our case, we are proceeding with the manipulation of the $\delta^{(2)}$ and $\delta^{(4)}$ coefficients.

Starting from the second-order term, we find that:

$$\delta^{(2)} = \frac{Q^2R^2}{2\left(1+R^2\right)}\left[ \left(C_1^x + 3C_2^x\right)^2 \tau_x^2 + \left(C_1^y + 3C_2^y\right)^2 \tau_y^2 - 1 \right], \quad (15)$$

where $R = \Delta y/\Delta x$, $\tau_x = \cos\theta$, $\tau_y = \sin\theta$, and $Q$ determines the time-step size, via:

$$\Delta t = \frac{QR\Delta x}{c_0\sqrt{1+R^2}}. \quad (16)$$

In (16), $Q = 1$ yields the well-known Yee's stability criterion. Clearly, the second-order term vanishes if:

$$C_1^u + 3C_2^u = 1,\ u = x,y, \quad (17)$$

In essence, (17) guarantees that the spatial operators are at least second-order accurate, which is necessary so that their error matches the corresponding temporal one.

The treatment of the $\delta^{(4)}$ term is more involved, as it is expressed according to:

$$\delta^{(4)}(\theta) = \frac{(QR)^4}{24\left(1+R^2\right)^2} - \frac{(QR)^2}{3072\left(1+R^2\right)^2}\Big[ 128\left(C_1^x + 27C_2^x\right)\tau_x^4 + 128R^4\left(C_1^y + 27C_2^y\right)\tau_y^4 + 128R^2\left(C_1^x + 27C_2^x\right)\tau_x^4 + 128R^2\left(C_1^y + 27C_2^y\right)\tau_y^4 + 3Q^2R^2\left(64\tau_x^4 + \tau_x^3\tau_y + 128\tau_x^2\tau_y^2 + \tau_x\tau_y^3 + 64\tau_y^4\right)\Big], \quad (18)$$

where (17) has already been partially substituted for simplicity. It is clear that $\delta^{(4)}$ cannot be eliminated, as the corresponding SS-FDTD scheme cannot accomplish fourth-order space-time accuracy. A more realistic goal is to render $\delta^{(4)}$ as small as possible, so that better overall performance is attained, compared to standard fourth-order spatial approximations. For this reason, (18) is rearranged, using the identities:

$$\tau_x^4 = \frac{3}{8} + \frac{1}{2}\cos(2\theta) + \frac{1}{8}\cos(4\theta), \quad (19)$$

$$\tau_y^4 = \frac{3}{8} - \frac{1}{2}\cos(2\theta) + \frac{1}{8}\cos(4\theta), \quad (20)$$

$$\tau_x^3\tau_y = \frac{1}{4}\sin(2\theta) + \frac{1}{8}\sin(4\theta), \quad (21)$$

$$\tau_x^2\tau_y^2 = \frac{1}{8} - \frac{1}{8}\cos(4\theta), \quad (22)$$

$$\tau_x\tau_y^3 = \frac{1}{4}\sin(2\theta) - \frac{1}{8}\sin(4\theta). \quad (23)$$

Taking (19)-(23) into account, $\delta^{(4)}$ is expressed as a finite trigonometric series, and two additional constraints can be derived from the vanishing of an equal number of terms. If the series' constant term is set equal to zero, the following equation is obtained:

$$C_1^x + 27C_2^x + R^2\left(C_1^y + 27C_2^y\right) = -\frac{4(QR)^2}{3(1+R^2)}. \quad (24)$$

The last equation is extracted from the coefficient of the $\cos(2\theta)$ term, resulting in:

$$C_1^x + 27C_2^x - R^2\left(C_1^y + 27C_2^y\right) = 0. \quad (25)$$

The solution of the system comprising (17), (24), and (25) yields the optimum spatial operators, whose final form takes into account the cell shape and the time-step size, as the resulting coefficient expressions are:

$$C_1^x = \frac{9}{8} + \frac{Q^2}{12}\frac{R^2}{1+R^2}, \; C_2^x = -\frac{1}{24} - \frac{Q^2}{36}\frac{R^2}{1+R^2}, \quad (26)$$

$$C_1^y = \frac{9}{8} + \frac{Q^2}{12}\frac{1}{1+R^2}, \; C_2^x = -\frac{1}{24} - \frac{Q^2}{36}\frac{1}{1+R^2}. \quad (27)$$

Consequently, the procedure followed herein concludes that the standard fourth-order operators are the most suitable choice, only if a very small time step (i.e., $Q \to 0$) is selected. This, however, is not the case in unconditionally-stable FDTD methods, and modified approximations that do not necessarily preserve the maximum order of accuracy can guarantee lower dispersion flaws.

## III. ASSESSMENT OF METHODOLOGY

The stability of the numerical scheme is revealed by obtaining the eigenvalues of its amplification matrix. The latter is equal to $[\mathbf{L}_A][\mathbf{L}_B]^2[\mathbf{L}_A]$, as defined in (6), (7), and its eigenvalues are: $\lambda_1 = 1$, and,

$$\lambda_{2,3} = \frac{w - 64v \pm \mathrm{j}16\sqrt{wv}}{r}, \quad (28)$$

where

$$w = \left(16 + c_0^2\Delta t^2 X^2\right)^2\left(16 + c_0^2\Delta t^2 Y^2\right)^2, \quad (29)$$

$$v = -64c_0^2\Delta t^2\left(X^2 + Y^2\right)\left(c_0^4\Delta t^4 X^2Y^2 + 256\right), \quad (30)$$

$$r = -c_0^2\Delta t^2\left(16 + c_0^2\Delta t^2 X^2\right)^2\left(16 + c_0^2\Delta t^2 Y^2\right)^2 \times\left(X^2 + Y^2\right)\left(c_0^4\Delta t^4 X^2Y^2 + 256\right). \quad (31)$$

It can be shown that the magnitude of $\lambda_{1,2,3}$ is 1, regardless of the time-step size. Hence, the specific SS-FDTD updates are unconditionally stable. An exemplary plot of the eigenvalues on the complex plane is given in Fig. 1 when $R$ = 1, the spatial density is 40 cells per wavelength, and $Q \le 50$. As expected, all values lie on the circumference of the unit circle.

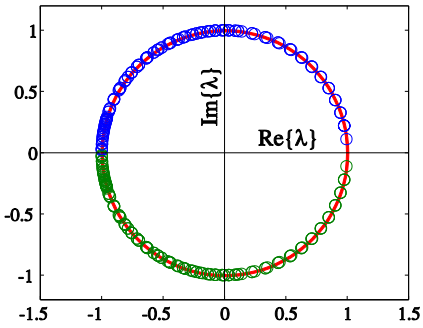


Fig. 1. Eigenvalues of the amplification matrix on the complex plane for various $\Delta t$.

Next, the algorithm's accuracy is assessed in terms of the dispersive error affecting the phase velocity, whose value $\tilde{c} = \omega/\tilde{k}$ is extracted from the dispersion relation (10), and the overall error is estimated from:

$$e_t = \frac{1}{2\pi c_0}\int_0^{2\pi}\left|c_0 - \tilde{c}\right| d\theta. \quad (32)$$

The positive impact of the modified operators on the scheme's accuracy is illustrated in Fig. 2, where the SS-FDTD method that applies standard fourth-order approximations is also depicted (time-steps five and ten times larger than Yee's stability limit are considered). The plotted curves reveal a significant error reduction that is not confined within specific frequency bands. In fact, the evidence show that a specific accuracy level can be now accomplished with twice as large a time-step, thanks to the sophisticated design of the algorithm, ensuring better utilization of computational resources.

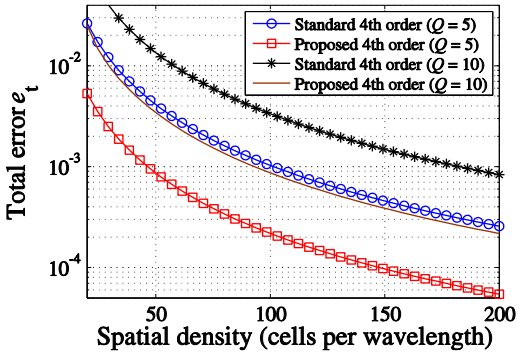


Fig. 2. Error $e_t$ versus mesh density for different $\Delta t$.

## IV. NUMERICAL RESULTS

The performance of the modified SS-FDTD algorithm

is evaluated considering an 8 cm × 6 cm cavity, bounded by perfectly conducting walls. First, we perform two sets of simulations, one for the $TE_{11}$ mode at 3.123 GHz and one for the $TE_{21}$ mode at 4.504 GHz. The computational space comprises 200 × 150 cells and tests are conducted for different time-step magnitudes. In essence, the maximum $L_2$ error of $H_z$ is recorded for a time period equivalent to 2000 iterations when $Q = 2$. The results are displayed in Table 1, where the standard fourth-order operators and the proposed ones are compared. It is verified that significant error cancellation is accomplished regardless of the time-step size. Specifically, accuracy is improved by 3.5 times in the first case, and by 4.2 times in the second case, verifying the potential of the new derivative approximation.

Using the same configuration as previously, the second test pertains to the detection of the structure's first 24 resonant frequencies. Now, an 80 × 60 grid is used, and simulations for 32768 time-steps with $Q = 5$ are performed. Figure 3 displays the absolute errors in the frequencies of the detected modes, and the superior spectral properties of the proposed SS-FDTD method are clearly illustrated. Specifically, the average error of the standard scheme is 55.07 MHz, which is suppressed to only 7.31 MHz by the modified operators.

Table 1: Maximum $L_2$ errors for different time-step sizes, in the cavity problems with single-mode support

| | $TE_{11}$ Mode | | $TE_{21}$ Mode | |
|---|---|---|---|---|
| $Q$ | Standard | Proposed | Standard | Proposed |
| 2 | $1.05\cdot10^{-3}$ | $2.94\cdot10^{-4}$ | $3.11\cdot10^{-3}$ | $7.31\cdot10^{-4}$ |
| 4 | $4.19\cdot10^{-3}$ | $1.18\cdot10^{-3}$ | $1.24\cdot10^{-2}$ | $2.92\cdot10^{-3}$ |
| 6 | $9.42\cdot10^{-3}$ | $2.65\cdot10^{-3}$ | $2.80\cdot10^{-2}$ | $6.59\cdot10^{-3}$ |
| 8 | $1.67\cdot10^{-2}$ | $4.72\cdot10^{-3}$ | $4.95\cdot10^{-2}$ | $1.17\cdot10^{-2}$ |
| 10 | $2.61\cdot10^{-2}$ | $7.38\cdot10^{-3}$ | $7.71\cdot10^{-2}$ | $1.84\cdot10^{-2}$ |

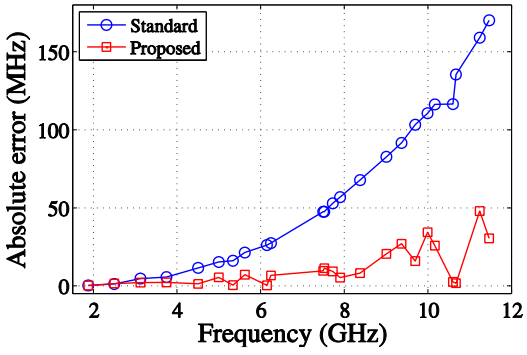


Fig. 3. Absolute error in detecting the resonant frequencies of a rectangular cavity.

## V. CONCLUSION

We have successfully remedied the accuracy of an unconditionally stable SS-FDTD method, by deriving modified spatial operators with three-cell stencils. The form of these approximations is determined via a design procedure that balances space-time errors over all frequencies better than standard formulae. The modified scheme outperforms its conventional counterpart, as it guarantees similar error levels with larger time-steps.

## REFERENCES

[1] K. S. Yee, "Numerical solution of initial boundary value problems involving Maxwell's equations in isotropic media," *IEEE Trans. Antennas Propag.*, vol. AP-14, pp. 302-307, 1966.

[2] A. Taflove and S. C. Hagness, *Computational Electrodynamics: The Finite-Difference Time-Domain Method*. Artech House, Norwood, MA, ed. 3, 2005.

[3] G. Sun and C. W. Trueman, "Accuracy of three unconditionally-stable FDTD schemes," *ACES J.*, vol. 18, no. 4, pp. 41-47, Nov. 2003.

[4] F. Zheng, Z. Chen, and J. Zhang, "A finite-difference time-domain method without the Courant stability conditions," *IEEE Microw. Guided Wave Lett.*, vol. 9, no. 11, pp. 441-443, Nov. 1999.

[5] J. Shibayama, M. Muraki, J. Yamauchi, and H. Nakano, "Efficient implicit FDTD algorithm based on locally one-dimensional scheme," *Electron. Lett.*, vol. 41, no. 19, pp. 1046-1047, Sept. 2005.

[6] J. Lee and B. Fornberg, "A split step approach for the 3-D Maxwell's equations," *J. Comp. Appl. Math.*, vol. 158, no. 2, pp. 485-505, Sept. 2003.

[7] W. Fu and E. L. Tan, "Development of split-step FDTD method with higher-order spatial accuracy," *Electron. Lett.*, vol. 40, no. 20, pp. 1252-1253, Sept. 2004.

[8] M. Kusaf and A. Y. Oztoprak, "An unconditionally stable split-step FDTD method for low anisotropy," *IEEE Microw. Wireless Comp. Lett.*, vol. 18, no. 4, pp. 224-226, Apr. 2008.

[9] A. Grande, J. A. Pereda, A. Serroukh, I. Barba, A. C. Cabeceira, and J. Represa, "Reinterpreting four-stage split-step FDTD methods as two-stage methods," *IEEE Trans. Antennas Propag.*, vol. 61, no. 11, pp. 5818-5821, Nov. 2013.

[10] D. Y. Heh and E. L. Tan, "Further reinterpretation of multi-stage implicit FDTD schemes," *IEEE Trans. Antennas Propag.*, vol. 62, no. 8, pp. 4407-4411, Aug. 2014.

[11] W. Fu and E. L. Tan, "A parameter optimized ADI-FDTD method based on the (2,4) stencil," *IEEE Trans. Antennas Propag.*, vol. 54, no. 6, pp. 1836-1842, June 2006.

[12] Q.-F. Liu, W.-Y. Yin, Z. Chen, and P.-G. Liu, "An efficient method to reduce the numerical dispersion in the LOD-FDTD method based on the (2,4) stencil," *IEEE Trans. Antennas Propag.*, vol. 58, no. 7, pp. 2384-2393, July 2010.

# A 3-D Polynomial-Chaos FDTD Technique for Complex Inhomogeneous Media with Arbitrary Stochastically-Varying Index Gradients

**Georgios G. Pyrialakos [1], Theodoros T. Zygiridis [2], and Nikolaos V. Kantartzis [1]**

[1] Department of Electrical and Computer Engineering
Aristotle University of Thessaloniki, Thessaloniki, 54124, Greece
pyrialak@auth.gr, kant@auth.gr

[2] Department of Informatics and Telecommunications Engineering
University of Western Macedonia, Kozani, 50100, Greece
tzygiridis@uowm.gr

***Abstract*** ─ An enhanced finite-difference time-domain algorithm featuring the polynomial chaos representation is introduced in this paper for problems with stochastic uncertainties. Focusing on the solution of the governing partial differential equations, the new 3-D method uses the Karhunen-Loève expansion to effectively decorrelate random input parameters denoted by stochastic processes. So, the space dimension is seriously reduced and high accuracy levels are attained, even for media with abrupt and fully unknown statistical variations. These profits are verified via a detailed numerical study.

***Index Terms*** ─ Advanced FDTD methods, polynomial chaos, random media, stochastic process, uncertainties.

## I. INTRODUCTION

The assessment of stochastic uncertainties, inherent in electromagnetics, has been of pivotal significance, so leading to different numerical schemes. Amid them the Monte Carlo (MC) approach [1], albeit accurate, has proven time-consuming, due to its excessively many realizations and slow convergence to the desired result. Recently, efficient techniques have been presented [2-6], such as the generalized polynomial chaos finite-difference time-domain (GPC-FDTD) algorithm [7, 8]. Usually, uncertainties emerge from discrete stochastic variables or processes that vary in an unknown way. Being difficult to model, the latter cannot be directly plugged in the GPC-FDTD technique, as they require an infinite number of correlated random variables.

To overcome such an issue, this paper develops a 3-D GPC-FDTD methodology for complex materials with arbitrary statistically-varying index gradients. The novel algorithm utilizes an orthogonal field expansion over the space of random parameters, so minimizing the error for both the mean value and variance. While it is primarily optimized for the extraction of the first two moments, the approximated relation between the output and stochastic parameter can provide with more valuable information like the computation of high-order statistical moments or maxima/minima, useful in electromagnetic compatibility (EMC) applications [9, 10]. To decrease the dimension of space spanned by the input parameters and decorrelate them, the Karhunen-Loève scheme is employed. It transforms the infinite product space of random inputs to be described by a new base that can be safely truncated. The resulting variables are, also, uncorrelated, which for Gaussian processes is equivalent to independence; an ample claim for the GPC applicability. Numerical outcomes certify our method, accelerated via graphics processor units (GPUs), and reveal its superiority.

## II. PROPOSED METHODOLOGY

### A. Generalized polynomial chaos expansion

The GPC method expands all fields in a summation of orthogonal, under an inner product, basis functions over space $\Omega = \cup\Omega_i$ ($i$ = 1,2,…,$D$), spanned by all $D$ random variables $\omega_i$ (each defined in $\Omega_i$), on condition that they are statistically independent. The orthogonality is satisfied with respect to the inner product:

$$\begin{aligned}\left\langle \Theta_a(\boldsymbol{\omega}), \Theta_b(\boldsymbol{\omega}) \right\rangle &\triangleq \int_{\Omega} \Theta_a(\boldsymbol{\omega}) \Theta_b(\boldsymbol{\omega}) w(\boldsymbol{\omega}) d\boldsymbol{\omega} \\ &= \left\langle \Theta_a(\boldsymbol{\omega}), \Theta_a(\boldsymbol{\omega}) \right\rangle \delta_{a,b},\end{aligned} \tag{1}$$

with $\Theta_{a,b}(\boldsymbol{\omega})$ the basis functions, $\boldsymbol{\omega} = [\omega_1,\omega_2,\ldots,\omega_D]^{\mathrm{T}}$ the vector formed by $\omega_i$, $\delta_{a,b}$ the Kronecker's delta, and $w(\boldsymbol{\omega})$ the distribution function of $\boldsymbol{\omega}$. Note that, in the case of a single random variable $\omega_i$, the most common $w(\omega_i)$ are related to well-known polynomials like the Hermite (Gaussian distribution), the Jacobi (beta distribution), and the Legendre (uniform distribution) polynomials. However, in the multivariate case, $\Theta_{a,b}(\boldsymbol{\omega})$ are generally unknown, unless a statistical independence between the random variables is guaranteed [8]. Only then $\Theta_{a,b}(\boldsymbol{\omega})$ may be expressed as the product of the prior polynomials related to their known distributions, i.e.,

*Submitted On: December 31, 2015*
*Accepted On: April 26, 2016*

$$\Theta_a(\boldsymbol{\omega}) = \prod_{i=1}^{D} \Theta_{a_i}(\omega_i), \tag{2}$$

where $\Theta_{ai}(\omega_i)$ is a univariate basis in $\omega_i$ of polynomial order $a_i$. So, any electric/magnetic component $F = \{E_x, E_y, E_z, H_x, H_y, H_z\}$ in the FDTD domain is written as:

$$F\big|_{i,j,k}^{n}(\boldsymbol{\omega}) = \sum_{a=0}^{P} f^a\big|_{i,j,k}^{n} \Theta_a(\boldsymbol{\omega}), \tag{3}$$

with $f^a$ the corresponding coefficients and $P$ the number of polynomials, calculated for the highest order $N$, by:

$$P = \binom{N+D}{N} = \frac{(D+N)!}{D!N!}. \tag{4}$$

Note that the GPC technique can not directly treat cases, where stochastic processes affect the output, since the latter are described by an infinite series of correlated random variables indexed by some physical coordinate. In contrast, the FDTD discretization can hardly offer any benefit, since one ends up with a very large (although not infinite) number of correlated random variables.

### B. Karhunen-Loève stochastic representation

To overcome these issues, we launch the Karhunen-Loève (KL) expansion [8] for both the dimension reduction and decorrelation of the stochastic processes. Let $Y_x(\boldsymbol{\omega})$ be a stochastic process varying over coordinate $x \in [p, q]$ bounded domain, with a covariance function of $C(x_1, x_2)$. The KL expansion of $Y_x(\boldsymbol{\omega})$ reads:

$$Y_x(\boldsymbol{\omega}) = m\{Y_x(\boldsymbol{\omega})\} + \sum_{i=0}^{\infty} \sqrt{\lambda_i}\, \psi_i(x) Y_i(\boldsymbol{\omega}), \tag{5}$$

where $m\{Y_x(\boldsymbol{\omega})\}$ is the mean value of $Y_x(\boldsymbol{\omega})$ and $Y_i(\boldsymbol{\omega})$ are centered, uncorrelated random variables of unit variance. Eigenfunctions $\psi_i(x)$ and their respective eigenvalues $\lambda_i$ are determined via the eigenvalue problem:

$$\int_{[p,q]} C(x,l)\psi_i(l)\, dl = \lambda_i \psi_i(x). \tag{6}$$

Note that for Gaussian processes, $Y_i(\boldsymbol{\omega})$ are generated as independent random variables. Also, when the process is stationary, i.e., its covariance can be written as $C(x_1, x_2) = C(x_2 - x_1)$, the solution of (6) is equivalent to the Fourier transform of $C(x)$, assuming it is periodic outside $[p, q]$. A key trait of the KL expansion (and a motive for its choice in our method) is the decay of $\lambda_i$ as $i$ increases. So, it is possible to describe the entire stochastic process with only a small truncated series of $Y_i(\boldsymbol{\omega})$.

### C. Enhanced GPC-FDTD update equations

The update equations of the 3-D algorithm are extracted by plugging (3) into the leapfrog formulas [9]. The stochastic process (randomness source) $Y_x(\boldsymbol{\omega})$, in the KL expansion (5), is the relative electric permittivity $\varepsilon_r(\boldsymbol{\omega})$, where $x$ can be any coordinate. By replacing $Y_i(\boldsymbol{\omega})$ with $\omega_i$ in (5), defining $\Omega$, and truncating the infinite sum up to a $K$ (KL truncation limit), we get:

$$M = m\{\varepsilon_r(\boldsymbol{\omega})\}\varepsilon_0 + \sum_{i=0}^{K} \sqrt{\lambda_i}\, \psi_i(x)\omega_i, \tag{7}$$

which is a very accurate approximation. For instance, the $E_z$ coefficients are given by:

$$\begin{aligned}\sum_{a=0}^{P} e_z^a\big|_{i,j,k+1/2}^{n+1} \Theta_a(\boldsymbol{\omega}) &= R_1 \sum_{a=0}^{P} e_z^a\big|_{i,j,k+1/2}^{n} \Theta_a(\boldsymbol{\omega}) \\ &+ R_2 \begin{bmatrix} \frac{1}{\Delta x}\sum_{a=0}^{P}\left( h_y^a\big|_{i+1/2,j,k+1/2}^{n+1/2} - h_y^a\big|_{i-1/2,j,k+1/2}^{n+1/2}\right)\Theta_a(\boldsymbol{\omega}) \\ -\frac{1}{\Delta y}\sum_{a=0}^{P}\left( h_x^a\big|_{i,j+1/2,k+1/2}^{n+1/2} - h_x^a\big|_{i,j-1/2,k+1/2}^{n+1/2}\right)\Theta_a(\boldsymbol{\omega}) \end{bmatrix},\end{aligned} \tag{8}$$

with $R_1 = (2M - \sigma'\Delta t)/(2M + \sigma'\Delta t)$, $R_2 = 2\Delta t/(2M + \sigma'\Delta t)$, and $\sigma'$ the losses. Due to (3), only the respective $e^a$ coefficients are involved. To derive the update equation for every $a$, we use a Galerkin process, which takes the inner product, as in (1), on both sides of (8) with the respective basis function. Thus, one arrives at:

$$\begin{aligned} e_z^a\big|_{i,j,k+1/2}^{n+1} &= \frac{1}{\theta}\sum_{b=0}^{P} e_z^b\big|_{i,j,k+1/2}^{n} \left\langle R_1\Theta_a(\boldsymbol{\omega}), \Theta_b(\boldsymbol{\omega})\right\rangle \\ &+ \frac{1}{\theta}\sum_{b=0}^{P}\begin{bmatrix} \frac{1}{\Delta x}\left( h_y^b\big|_{i+1/2,j,k+1/2}^{n+1/2} - h_y^b\big|_{i-1/2,j,k+1/2}^{n+1/2}\right) \\ -\frac{1}{\Delta y}\left( h_x^b\big|_{i,j+1/2,k+1/2}^{n+1/2} - h_x^b\big|_{i,j-1/2,k+1/2}^{n+1/2}\right)\end{bmatrix}, \\ &\cdot\left\langle R_2\Theta_a(\boldsymbol{\omega}), \Theta_b(\boldsymbol{\omega})\right\rangle \end{aligned} \tag{9}$$

for $\theta = \langle\Theta_a(\boldsymbol{\omega}), \Theta_a(\boldsymbol{\omega})\rangle$, while similar expressions hold for the other components. Note that the stability of the algorithm is specified by the usual Courant condition, which yields flexible time-steps and is proven remarkably efficient (also stated in [7]), as no late-time instabilities were observed in any of our simulations. Consequently and along with the scheme's enhanced dispersion behavior, cases with challenging variations are precisely handled.

All inner products in (9) hold only in the region with the random medium and reduce to $\delta_{a,b}$ elsewhere. Their evaluation is conducted (prior the FDTD update) for each coordinate in the region and is trivial for up to second order of the KL limit $K$. For higher-order approximations, (1) may be split into 1-D integrals, on condition that (2) holds. Therefore, via a Taylor series expansion of $\omega_i$ in every inner product of (9), for an arbitrarily large order $s_i$ (even up to 10 is viewed trivial), we compute:

$$I_{s_i}^{a_i,b_i} = \int_{\Omega_i} \omega_i^{s_i}\, \Theta_{a_i}(\omega_i)\, \Theta_{b_i}(\omega_i)\, w(\omega_i)\, d\omega_i \ , \tag{10}$$

only once, and apply the Taylor expansion. For example, the second inner product in (9) is expressed as:

$$\left\langle R_2\Theta_a(\boldsymbol{\omega}), \Theta_b(\boldsymbol{\omega})\right\rangle = \sum_{s_1}^{D_T}\sum_{s_2}^{D_T}\cdots\sum_{s_K}^{D_T} T_{s_1,s_2,\ldots,s_K} \prod_{d=1}^{D} I_{s_d}^{a_d,b_d}, \tag{11}$$

with $T_s$ the respective Taylor coefficients and $D_T$ the maximum Taylor series order. As a consequence, extra accuracy can be consistently accomplished.

## III. GPU/CUDA IMPLEMENTATION

For its acceleration, the 3-D algorithm is parallelized for GPUs via the CUDA platform [11, 12], where different code parts are optimized for enhanced thread concurrency. As the coalescing mechanism is critical, all GPC coefficient matrices are accessed throughout the kernel code. Also, read-only matrices in each kernel are accessed through the texture buffer to increase performance. Then, the shared memory is used to load the pre-calculated inner products for all threads related to spatial coordinates that exhibit material stochasticity. For the 3-D convolution perfectly matched layers (CPMLs) [9], diverse kernels are initialized for each side and field component, executed concurrently by different streams. Hence, the proper grid and block alignment for every kernel is separately fulfilled. To evade errors at mesh corners, we use advanced atomic operators [6]. The acceleration of GPU codes compared to their conventional CPU (serialized) realizations, exceeds the promising value of 50 times.

## IV. NUMERICAL RESULTS

The new technique is validated via 3-D setups terminated by 8-cell CPMLs. We examine a $z$-directed wire current source that illuminates an infinite planar dielectric surface at the $y = 0$ plane, featuring a non-uniform (toward $x$ direction) stochastic permittivity (Fig. 1 (a)). The distribution function follows the Gaussian norm, hence Hermite polynomials are used as the basis functions. Also, the statistical moments of a domain point occupied by the random medium are $m\{\varepsilon_r\} = 3$ for the mean value and $\sigma\{\varepsilon_r\} = 0.02\ m\{\varepsilon_r\}$ for the standard deviation. Our correlation function is defined as $C(x - t) = e^{-(|x-t|/\alpha)}$, with $\alpha$ the correlation length, while higher $a$ translate to larger variations between neighboring points. The problem is divided into 317×317×317 cells, whose size is fixed and equal to the one tenth of the wavelength corresponding to the central frequency of the Gaussian excitation pulse. Also, the time increment is set at the level of 100-150 psec via the Courant condition, while the MC-FDTD scheme gives the reference solution. It generates 5000 different stochastic processes for the dielectric scattering surface. The determined confidence intervals, considered from a 10000 realization reference, do not exceed the 10% and 1% mark for 1000 and 5000 simulations respectively. Any choice beyond this level results in a marginal improvement. Figure 1 (a) depicts three stochastic processes for $\alpha = 0.5$ and Fig. 1 (b) shows the first five eigenfunctions $\psi_i(x)$ produced by the eigenvalue problem (6). The weighted addition of the infinite series of polynomials gives exactly the spatial variation of the dielectric slab. Thus, a higher $K$ order, including up to the $K$th eigenfunction, accounts for larger spatial variations. As these play a decreasingly serious role due to the nature of the electromagnetic wave solution the truncation is safely justified.

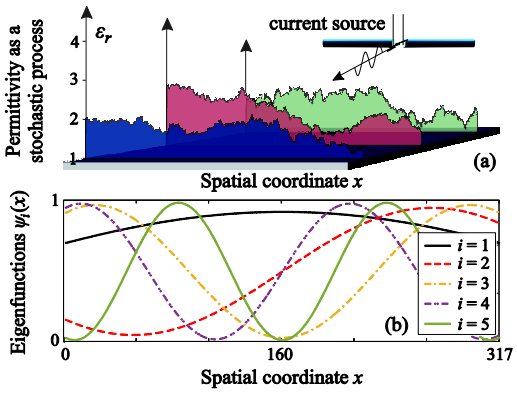


Fig. 1. (a) Perspective 3-D view of the simulation setup with the randomly generated stochastic processes, and (b) eigenfunctions $\psi_i(x)$ for $C(x - t) = e^{-(|x-t|/\alpha)}$ and $\alpha = 0.5$.

We, next, solve the problem for a KL limit up to $K = 3$ ($\alpha = 0.5$, $N = 3$). The choice of $N$ is justified as the best compromise between accuracy and computational efficiency. Also, for larger $K$ the system burden does not seem to justify the poor increase in accuracy. Figure 2 gives the electric field variance, where the plotted curves are snapshotted at a time-step near the peak of the Gaussian pulse, along the white line of the inlet figure. A clear improvement is attained as $K$ augments, yet the difference between the $K = 2$ and 3 curve is very small.

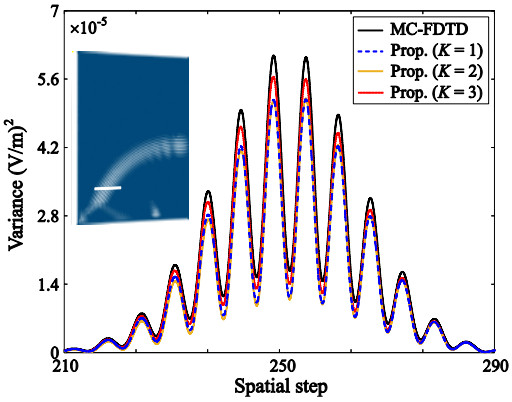


Fig. 2. Electric field variance via 5000 MC-FDTD runs and the proposed method for $\alpha = 0.5$ and $N = 3$.

Finally, Fig. 3 presents the variance of the electric field for $\alpha = 0.5$, yet with a prefixed $K = 4$ and a variety of GPC orders $N$. Apparently, convergence is slower in this case, revealing that the KL truncation limit has a more substantial impact compared to that of $N$. In contrast, it seems that the opposite situation holds for higher correlation length values of the random medium dielectric permittivity, where it is better to optimize $N$ in an effort to accomplish the desired approximation.

The main benefit of our algorithm is that via the GPC-KL formulation, one gets a similar approximation

order as with the MC-FDTD approach. While the latter requires thousands of FDTD solutions, the complexity of the former (analogous to *P*) is lower by two magnitude orders. Thus, we can reach a sufficient convergence by analyzing simulations with ascending *K* and *L* orders and keep the efficiency over an exact MC study. It is true, however, that memory can be up to two or even five to ten times higher, in relation with *K* and *L*. So, when memory is not an issue, the GPC-KL method is a powerful alternative. The GPU/CUDA implementation, while it does not add to the theoretical analysis, it is essential for the results assessment in rational times and so it is fully preferred over CPU for both methods.

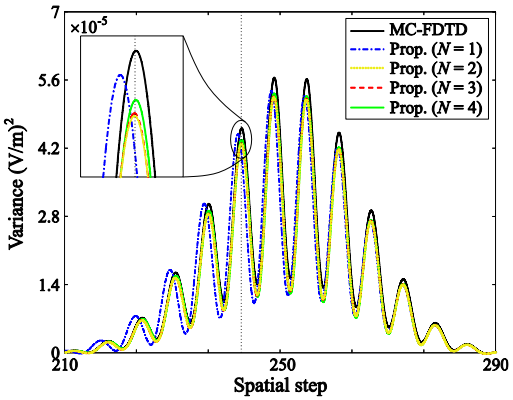


Fig. 3. Electric field variance via 5000 MC-FDTD runs and the proposed method for $\alpha$ = 0.5 and $K$ = 4.

## V. CONCLUSION

The rigorous modeling of inhomogeneous materials with complex statistical index gradients, is presented in this paper via a consistent 3-D GPC-FDTD method. The 3-D technique utilizes the efficient Karhunen-Loève expansion to handle the arbitrary stochastic processes. Results prove the profits of the proposed concept.

## REFERENCES

[1] F. Hastings, J. Schneider, and S. Broschat, "A Monte Carlo FDTD technique for rough surface scattering," *IEEE Trans. Antennas Propag.*, vol. 43, no. 11, pp. 1183-1191, Nov. 1995.

[2] M. Wong, J. Carette, A. Hadjem, and J. Wiart, "Stochastic electromagnetic modeling with uncertain dielectric properties using FDTD," in *Proc. 24th ACES Conf.*, pp. 450-455, 2008.

[3] M. Gilbert and F. Teixeira, "A small-perturbation automatic-differentiation method for uncertainty in electromagnetics," *IEEE Trans. Antennas Propag.*, vol. 60, no. 11, pp. 5305-5314, Nov. 2012.

[4] T. Tan, A. Taflove, and V. Backman, "Single realization stochastic FDTD for weak scattering waves in biological random media," *IEEE Trans. Antennas Propag.*, vol. 61, no. 2, pp. 818-828, 2013.

[5] B. T. Nguyen, C. Furse, and J. J. Simpson, "A 3-D stochastic FDTD model electromagnetic propagation in ionosphere plasma," *IEEE Trans. Antennas Propag.*, vol. 63, no. 1, pp. 304-313, 2015.

[6] G. Pyrialakos, T. Zygiridis, N. Kantartzis, and T. Tsiboukis, "GPU-based calculation of lightning-generated fields in 3D problems with statistically defined uncertainties," *IEEE Trans. Electromagn. Compat.*, vol. 57, no. 6, pp. 1556-1567, Dec. 2015.

[7] A. Austin and C. Sarris, "Efficient analysis of geometrical uncertainty in the FDTD ethod using PC for microwave circuits," *IEEE Trans. Microw. Theory Tech.*, vol. 61, no. 12, pp. 4293-4301, 2012.

[8] D. Xiu and G. Karniadakis, "The Wiener-Askey polynomial chaos for stochastic equations," *SIAM J. Sci. Comput.*, vol. 24, no. 2, pp. 619-644, 2002.

[9] A. Taflove and S. C. Hagness, *Computational Electrodynamics: The Finite-Difference Time-Domain Method*. Artech House, Boston, MA, 2005.

[10] H. W. Ott, *Electromagnetic Compatibility Engineering*. Wiley, New York, NY, 2009.

[11] V. Demir and A. Z. Elsherbeni, "Compute unified device architecture (CUDA) based finite-difference time-domain (FDTD) implementation," *ACES J.*, vol. 25, no. 4, pp. 303-314, Apr. 2010.

[12] A. Capozzoli, C. Curcio, G. D'Elia, A. Liseno, and P. Vinetti, "Fast CPU/GPU pattern evaluation of irregular arrays," *ACES J.*, vol. 2, pp. 355-272, 2010.

**APPLIED COMPUTATIONAL ELECTROMAGNETICS SOCIETY EXPRESS JOURNAL**
**http://aces-society.org**

# INFORMATION FOR AUTHORS

## PUBLICATION CRITERIA

Each paper is required to manifest some relation to applied computational electromagnetics. **Papers may address general issues in applied computational electromagnetics, or they may focus on specific applications, techniques, codes, or computational issues.** While the following list is not exhaustive, each paper will generally relate to at least one of these areas:

1. **Code validation.** This is done using internal checks or experimental, analytical or other computational data. Measured data of potential utility to code validation efforts will also be considered for publication.

2. **Code performance analysis.** This usually involves identification of numerical accuracy or other limitations, solution convergence, numerical and physical modeling error, and parameter tradeoffs. However, it is also permissible to address issues such as ease-of-use, set-up time, run time, special outputs, or other special features.

3. **Computational studies of basic physics.** This involves using a code, algorithm, or computational technique to simulate reality in such a way that better, or new physical insight or understanding, is achieved.

4. **New computational techniques** or new applications for existing computational techniques or codes.

5. **"Tricks of the trade"** in selecting and applying codes and techniques.

6. **New codes, algorithms, code enhancement, and code fixes.** This category is self-explanatory, but includes significant changes to existing codes, such as applicability extensions, algorithm optimization, problem correction, limitation removal, or other performance improvement. **Note: Code (or algorithm) capability descriptions are not acceptable, unless they contain sufficient technical material to justify consideration.**

7. **Code input/output issues.** This normally involves innovations in input (such as input geometry standardization, automatic mesh generation, or computer-aided design) or in output (whether it be tabular, graphical, statistical, Fourier-transformed, or otherwise signal-processed). Material dealing with input/output database management, output interpretation, or other input/output issues will also be considered for publication.

8. **Computer hardware issues.** This is the category for analysis of hardware capabilities and limitations of various types of electromagnetics computational requirements. Vector and parallel computational techniques and implementation are of particular interest.

Applications of interest include, but are not limited to, antennas (and their electromagnetic environments), networks, static fields, radar cross section, inverse scattering, shielding, radiation hazards, biological effects, biomedical applications, electromagnetic pulse (EMP), electromagnetic interference (EMI), electromagnetic compatibility (EMC), power transmission, charge transport, dielectric, magnetic and nonlinear materials, microwave components, MEMS, RFID, and MMIC technologies, remote sensing and geometrical and physical optics, radar and communications systems, sensors, fiber optics, plasmas, particle accelerators, generators and motors, electromagnetic wave propagation, non-destructive evaluation, eddy currents, and inverse scattering.

Techniques of interest include but not limited to frequency-domain and time-domain techniques, integral equation and differential equation techniques, diffraction theories, physical and geometrical optics, method of moments, finite differences and finite element techniques, transmission line method, modal expansions, perturbation methods, and hybrid methods.

Where possible and appropriate, authors are required to provide statements of quantitative accuracy for measured and/or computed data. This issue is discussed in "Accuracy & Publication: Requiring, quantitative accuracy statements to accompany data," by E. K. Miller, ACES Newsletter, Vol. 9, No. 3, pp. 23-29, 1994, ISBN 1056-9170.

## SUBMITTAL PROCEDURE

All submissions should be uploaded to ACES server through ACES web site (http://aces-society.org) by using the upload button, Express Journal section. Only pdf files are accepted for submission. The file size should not be larger than 6MB, otherwise permission from the Editor-in-Chief should be obtained first. Automated acknowledgment of the electronic submission, after the upload process is successfully completed, will be sent to the corresponding author only. It is the responsibility of the corresponding author to keep the remaining authors, if applicable, informed. Email submission is not accepted and will not be processed.

## EDITORIAL REVIEW

**In order to ensure an appropriate level of quality control**, papers are peer reviewed. They are reviewed both for technical correctness and for adherence to the listed guidelines regarding information content and format.

## PAPER FORMAT

Only camera-ready electronic files are accepted for publication. The term **"camera-ready" means that the material is neat, legible, reproducible, and in accordance with the final version format listed below.**

The following requirements are in effect for the final version of an ACES Express Journal paper:

1. The paper title should not be placed on a separate page. The title, author(s), abstract, and (space permitting) beginning of the paper itself should all be on the first page. The title, author(s), and author affiliations should be centered (center-justified) on the first page. The title should be of font size 14 and bolded, the author names should be of font size 12 and bolded, and the author affiliation should be of font size 10 (regular font, neither italic nor bolded).

2. An abstract is required. The abstract should be a brief summary of the work described in the paper. It should state the computer codes, computational techniques, and applications discussed in the paper (as applicable) and should otherwise be usable by technical abstracting and indexing services. The word "Abstract" has to be placed at the left margin of the paper, and should be bolded and italic. It also should be followed by a hyphen (–) with the main text of the abstract starting on the same line.

3. All section titles have to be centered and all the title letters should be written in caps. The section titles need to be numbered using roman numbering (I. II. ….)

4. Either British English or American English spellings may be used, provided that each word is spelled consistently throughout the paper.

5. Internal consistency of references format should be maintained. As a guideline for authors, we recommend that references be given using numerical numbering in the body of the paper (with numerical listing of all references at the end of the paper). The first letter of the authors' first name should be listed followed by a period, which in turn, followed by the authors' complete last name. Use a comma (,) to separate between the authors' names. Titles of papers or articles should be in quotation marks (" "), followed by the title of the journal, which should be in italic font. The journal volume (vol.), issue number (no.), page numbering (pp.), month and year of publication should come after the journal title in the sequence listed here.

6. Internal consistency shall also be maintained for other elements of style, such as equation numbering. Equation numbers should be placed in parentheses at the right column margin. All symbols in any equation have to be defined before the equation appears or right immediately following the equation.

7. The use of SI units is strongly encouraged. English units may be used as secondary units (in parentheses).

8. Figures and tables should be formatted appropriately (centered within the column, side-by-side, etc.) on the page such that the presented data appears close to and after it is being referenced in the text. When including figures and tables, all care should be taken so that they will appear appropriately when printed in black and white. For better visibility of paper on computer screen, it is good to make color figures with different line styles for figures with multiple curves. Color should also be tested to insure their ability to be distinguished after black and white printing. Avoid the use of large symbols with curves in a figure. It is always better to use different line styles such as solid, dotted, dashed, etc.

9. A figure caption should be located directly beneath the corresponding figure, and should be fully justified.

10. The intent and meaning of all text should be clear. For authors who are not masters of the English language, the ACES Editorial Staff will provide assistance with grammar (subject to clarity of intent and meaning). However, this may delay the scheduled publication date.

11. Unused space should be minimized. Sections and subsections should not normally begin on a new page.

ACES reserves the right to edit any uploaded material, however, this is not generally done. It is the author(s) responsibility to provide acceptable camera-ready files in pdf and MSWord formats. Incompatible or incomplete files will not be processed for publication, and authors will be requested to re-upload a revised acceptable version.

**COPYRIGHTS AND RELEASES**

Each primary author must execute the online copyright form and obtain a release from his/her organization vesting the copyright with ACES. Both the author(s) and affiliated organization(s) are allowed to use the copyrighted material freely for their own private purposes.

Permission is granted to quote short passages and reproduce figures and tables from an ACES Express Journal issue provided the source is cited. Copies of ACES Express Journal articles may be made in accordance with usage permitted by Sections 107 or 108 of the U.S. Copyright Law. The consent does not extend to other kinds of copying, such as for general distribution, for advertising or promotional purposes, for creating new collective works, or for resale. The reproduction of multiple copies and the use of articles or extracts for commercial purposes require the consent of the author and specific permission from ACES. Institutional members are allowed to copy any ACES Express Journal issue for their internal distribution only.

**PUBLICATION CHARGES**

There is a $200 basic publication charge assigned to each paper for ACES members, and $300 charge for non-ACES members. Corresponding authors should be active members of the society at the time of submission and the time of publication in order to receive the reduced charge.

ACES Express Journal doesn't allow for more than four pages. All authors must comply with the page limitations. ACES Express Journal is an online journal, and printed copies are not available.

**Upon completion of its first year, ACES Express Journal will be abstracted in INSPEC, in Engineering Index, DTIC, Science Citation Index Expanded, the Research Alert, and to Current Contents/Engineering, Computing & Technology.**